The Abdus Salam
International Centre
for Theoretical Physics
50th Anniversary 1964–2014

2585-18

Joint ICTP-TWAS School on Coherent State Transforms, Time-Frequency and Time-Scale Analysis, Applications

2 - 20 June 2014

Wavelet techniques for the imaging of the structure and dynamics of living cells

F. Argoul
ENS, Lyon, France

Wavelet techniques for the imaging of the structure and dynamics of living cells

F. Argoul, L. Berguiga, C. Martinez, E. Provera, L. Streppa
A. Arneodo, J. Elezgaray[*], *
B. Laperrousaz, V. Maguer-Satta[**], *T. Voeltzel*[**]

UMR5672 CNRS, Physics Laboratory - ENS Lyon
[*] UMR5248 CNRS-Université Bordeaux 1, Pessac
[**] CRCL, Research Center for Cancer of Lyon, CLB Lyon.

Lyon : at the cross-roads of Europe

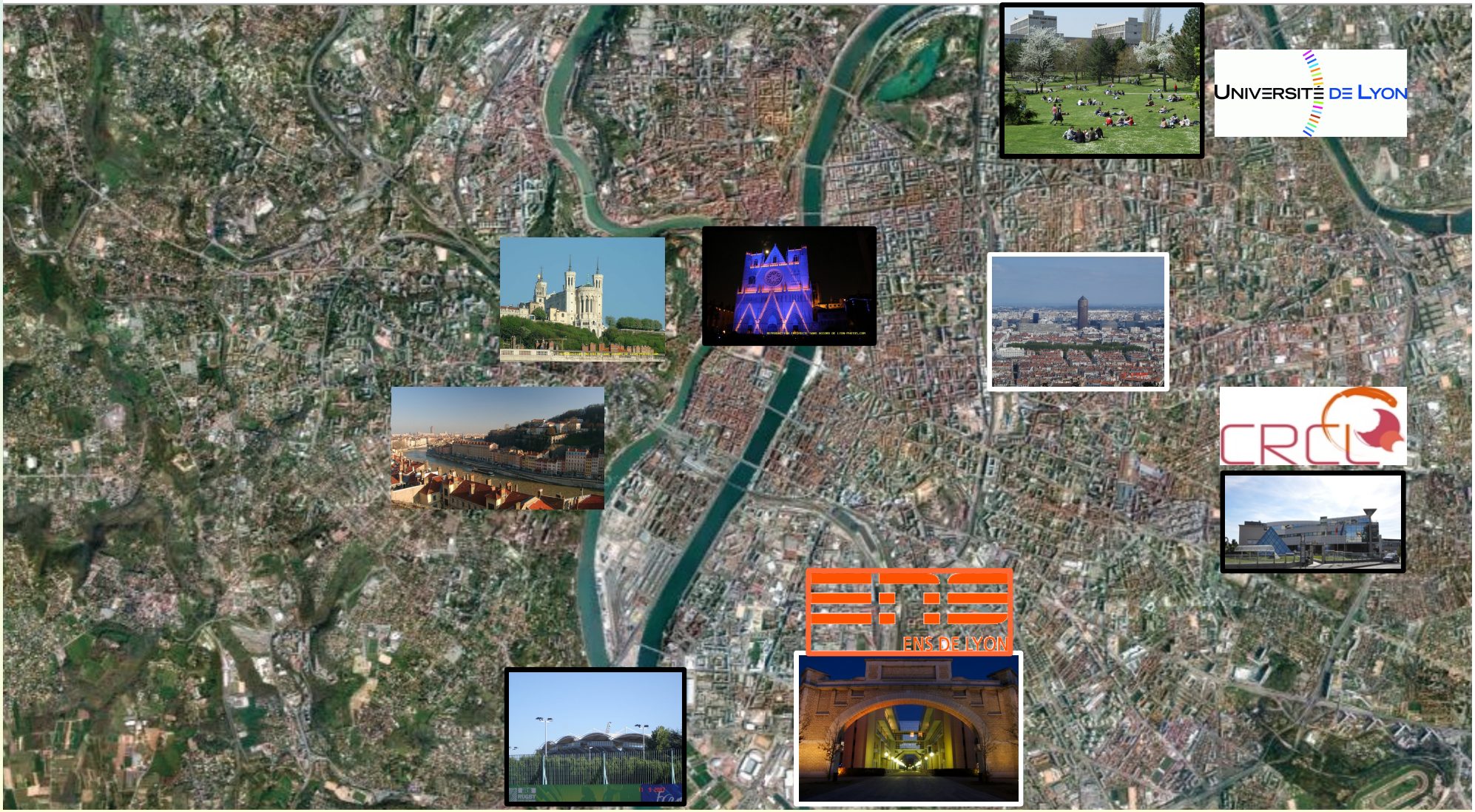

MANY THANKS to

L. Berguiga, S. Digiuni, C. Martinez, E. Boyer-Provera, L. Streppa

A. Arneodo, B. Audit, A. Devin[g],J. Elezgaray[g],

B. Laperrousaz, V. Maguer-Satta[g g], L. Schaeffer, T. Voeltzel[g g]

Physical approaches of biological systems: a question of spatial and temporal scales

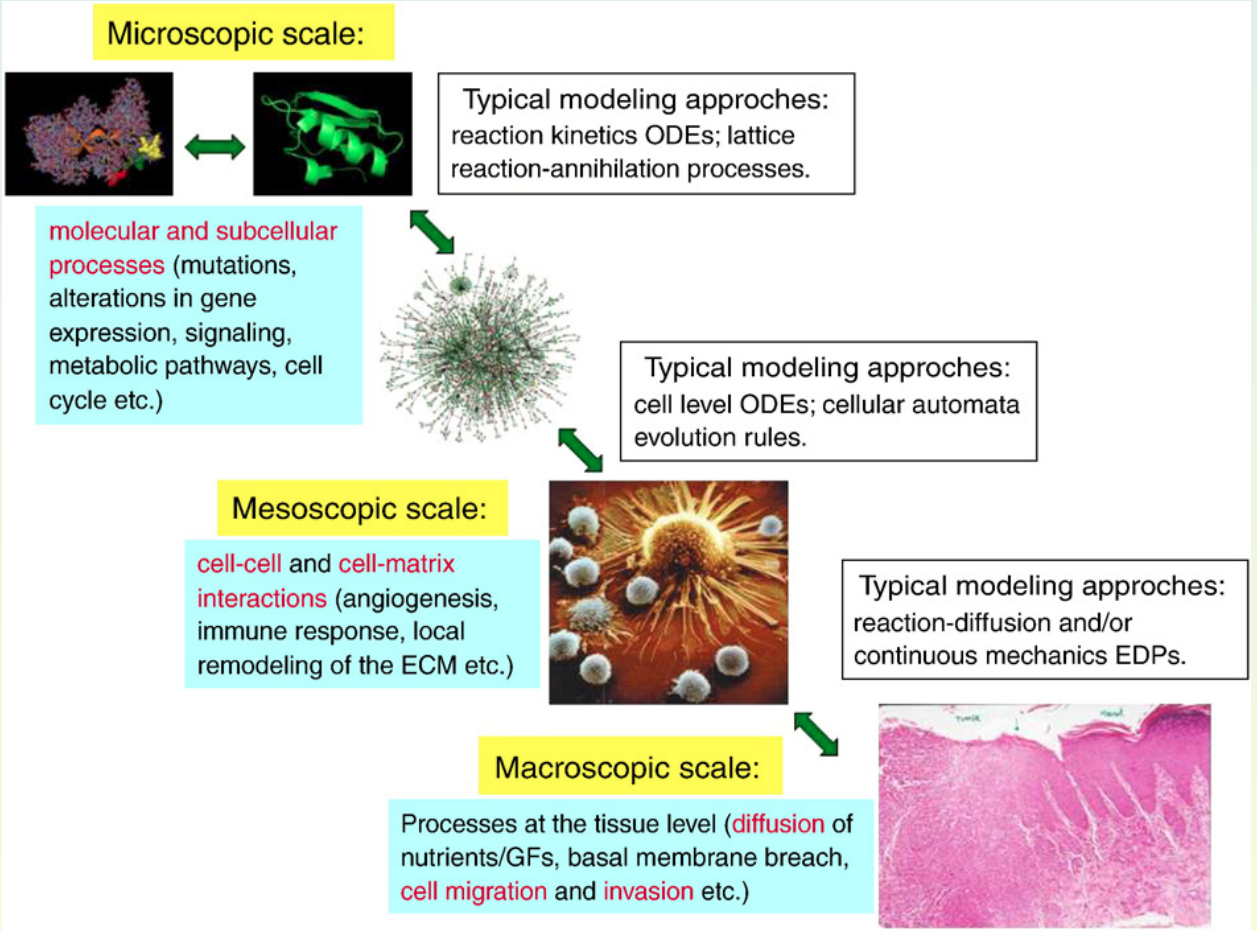

Hierarchy of scales and the related mechanisms and modeling approaches. The arrows indicate the mutual interdependence between the levels in multiscale modeling of cancer growth, implying that models/subsystems at a given scale use information from another scales.
[M. Ferreira Villela Cur. Op. Col. Interf. 2010]

Phase contrast microscopy

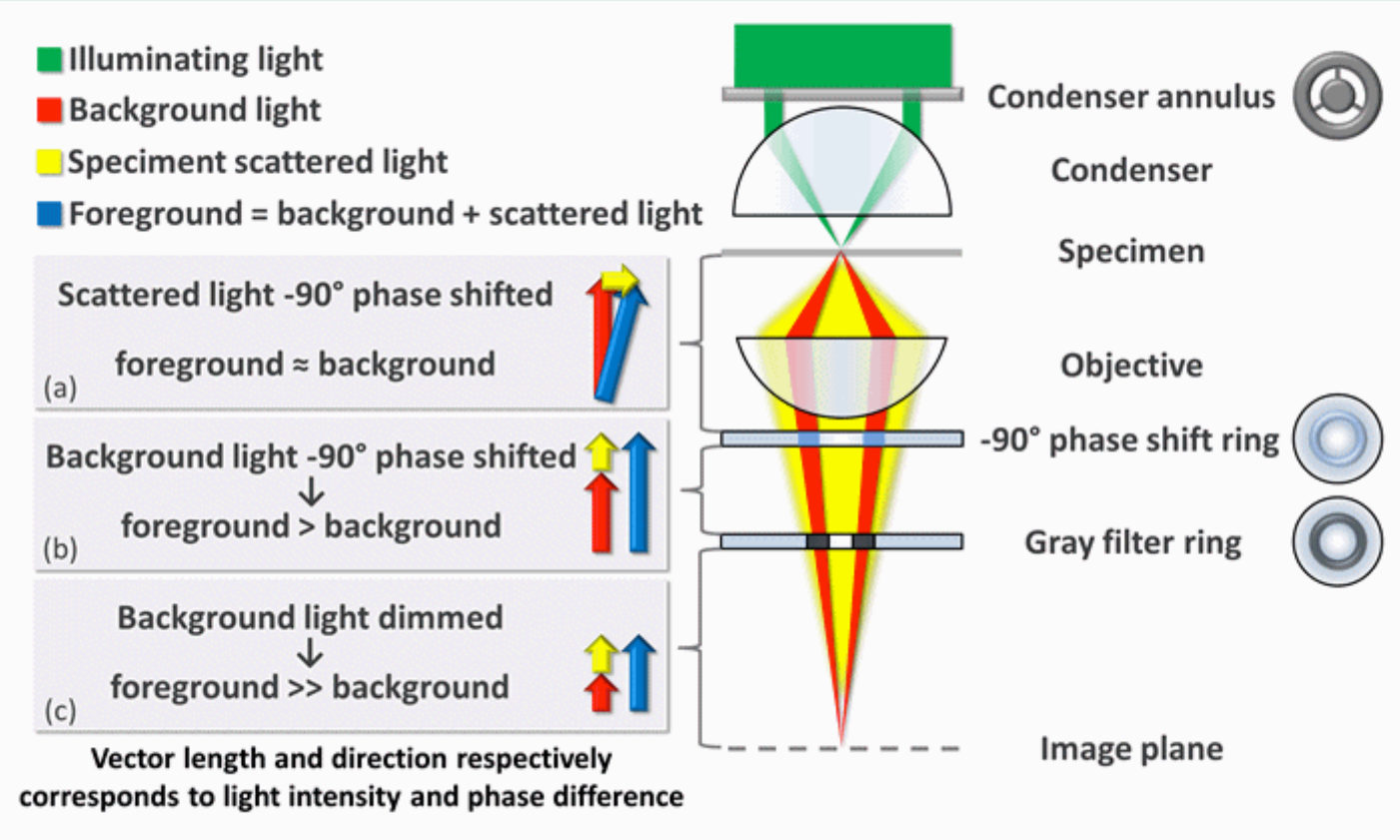

The basic principle of phase contrast microscopy (in the illustration we see a negative contrast system) is to separate the illuminating background light from the specimen scattered light, which make up the foreground details, and to manipulate them differently to enhance the contrast of the final image. (Fritz Zernike, Physica 9 (7): 686–698 (1942))

Phase contrast image

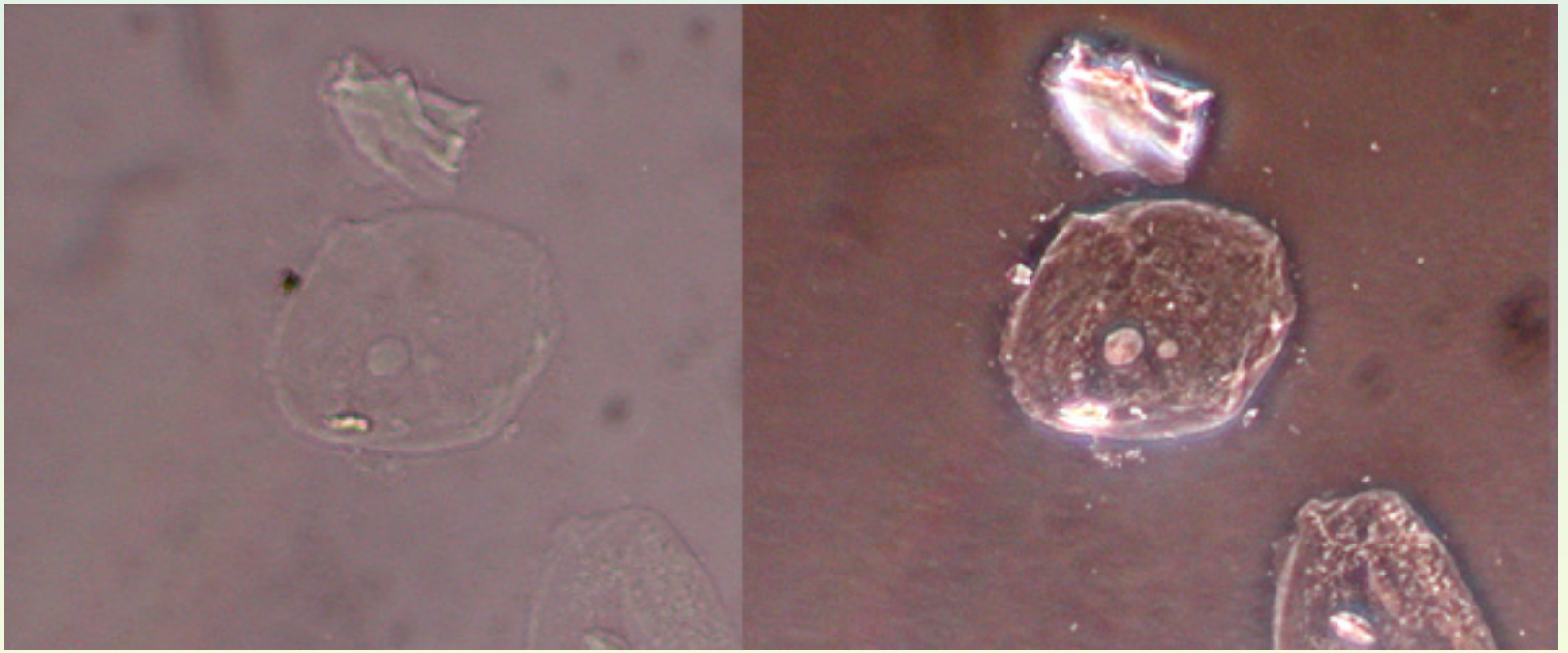

Negative phase contrast microscopy (right) image of a cell compared to traditional bright field microscopy (left).

Phase Contrast imaging of mesenchymal stem cells (MSCs)

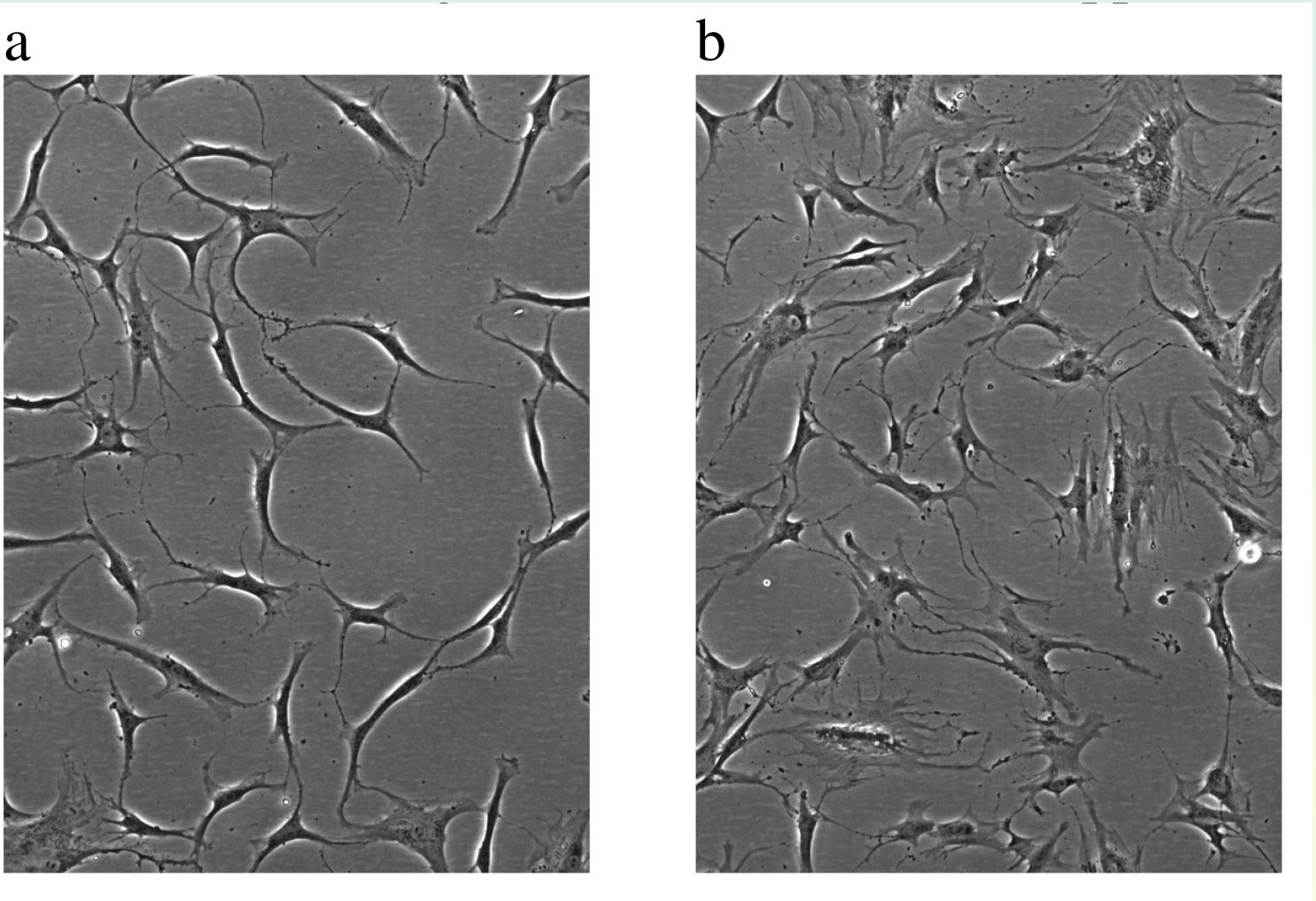

Mesenchymal stem cells, or MSCs, are multipotent stromal cells that can differentiate into a variety of cell types, including: osteoblasts (bone cells), chondrocytes (cartilage cells), and adipocytes (fat cells). *[Christopher J. Bradhurst - IEEE 2008]*

Differential interference contrast (DIC) microscopy

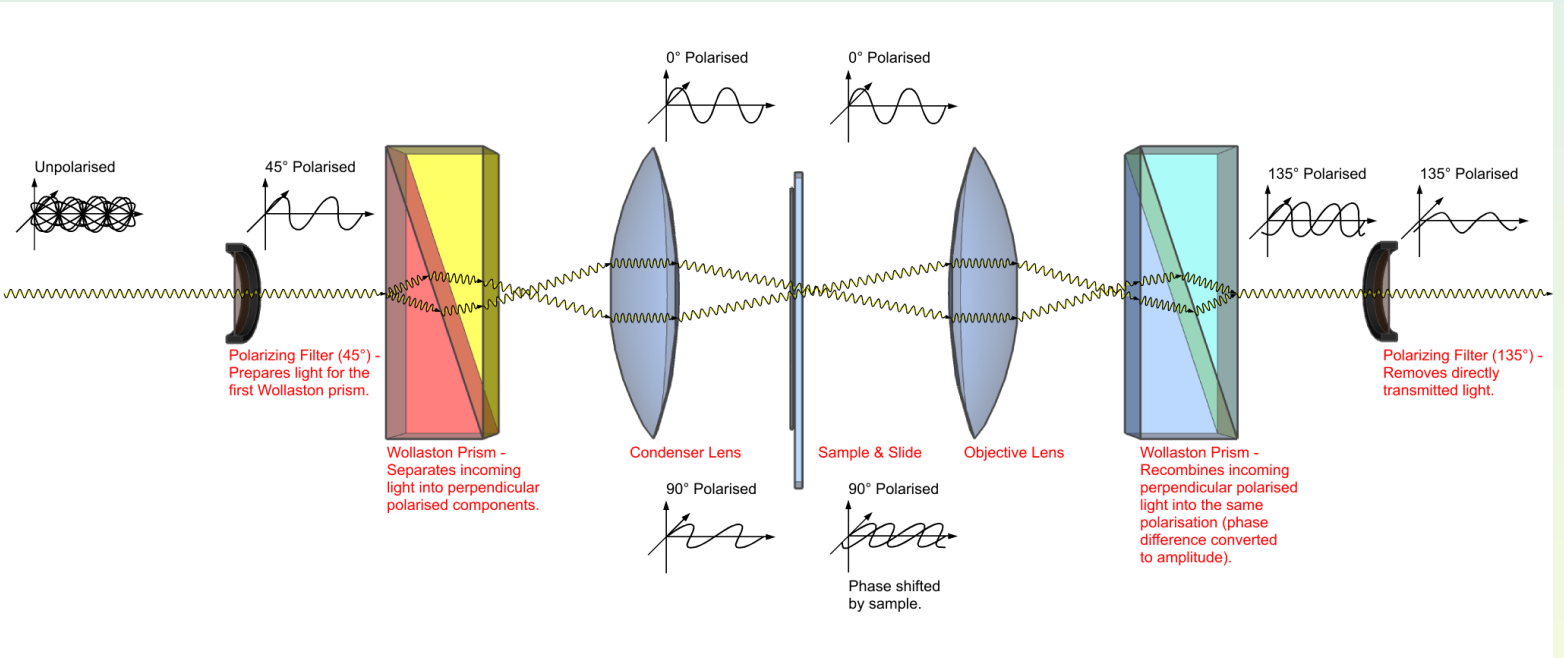

DIC works by separating a polarized light source into two orthogonally polarized mutually coherent parts which are spatially displaced (sheared) at the sample plane, and recombined before observation. Because the difference in phase is due to the difference in optical path length, this recombination of light causes "optical differentiation" of the optical path length, generating the image seen. (Nomarski 1950-1960)

Differential interference contrast (DIC) microscopy

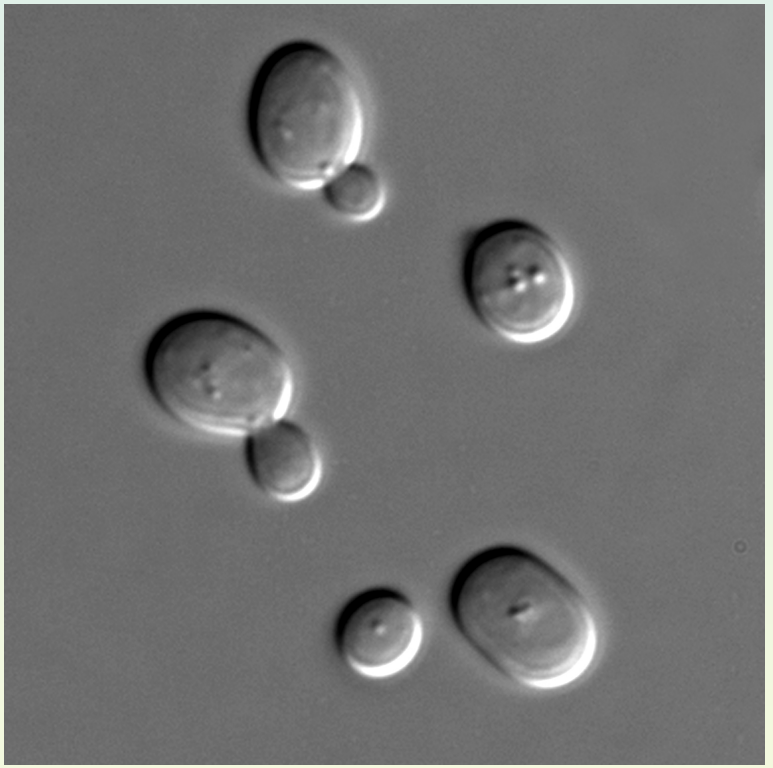

In 1952 Georges Nomarski patented what is today known as differential interference contrast (DIC) microscopy. It enhances contrast by creating artificial shadows, as if the object is illuminated from the side. But, to achieve this DIC microscopy uses polarized light, making it unsuitable when the object or its container alter polarization. In both Zernike and Normaski systems, the phase to amplitude conversion is nonlinear and there are significant artifacts in the images such as the halo in phase contrast and the disappearance of contrast along the direction perpendicular to shear in DIC. Quantitative phase imaging is not feasible with these techniques.

Quantitative reflection contrast microscopy of living cells

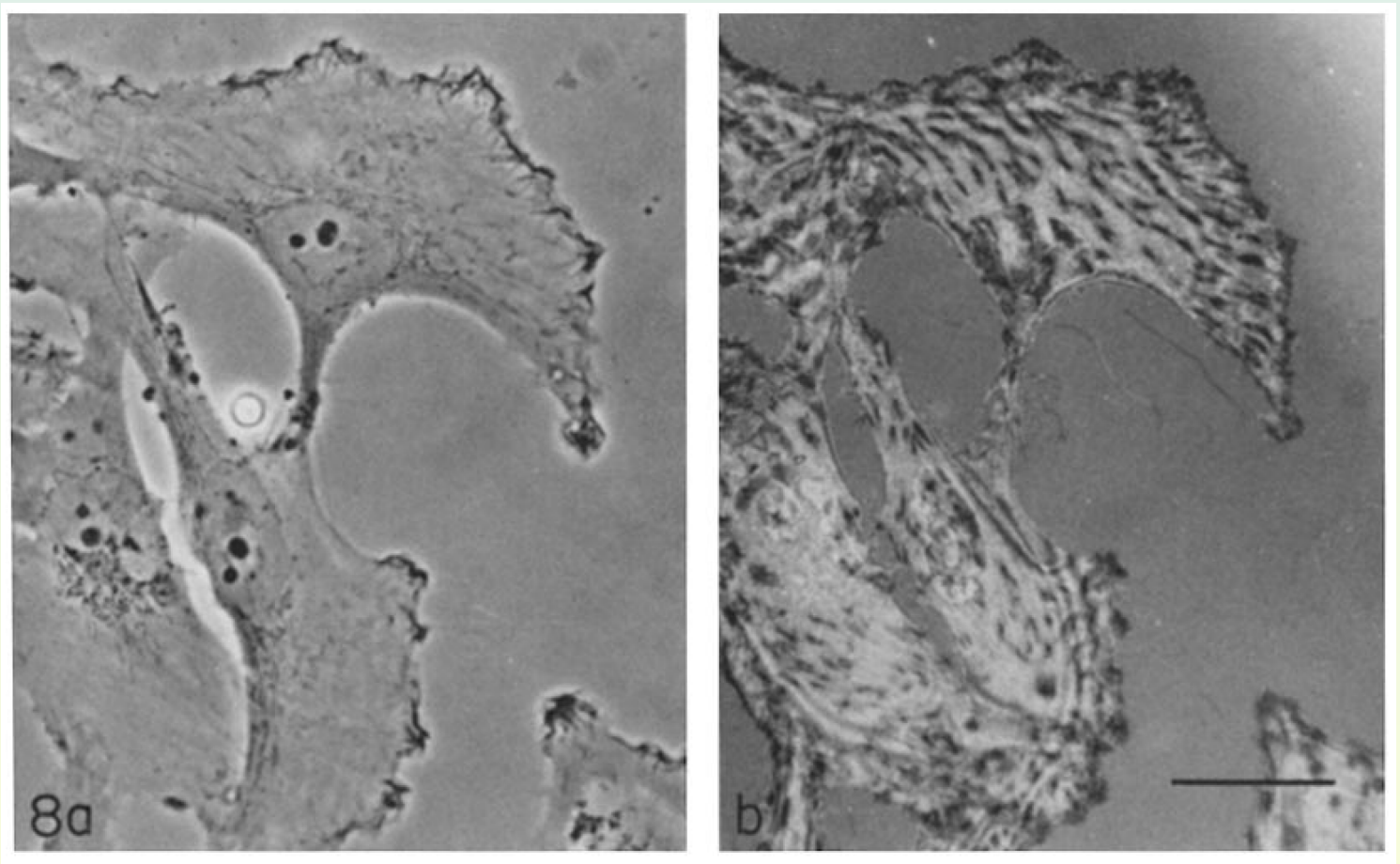

Human glioma cells. (a) phase contrast. (b) reflection contrast. In b, attachment plaques are clearly visible, while the ruffling (on the medium side of the cell) is only seen in phase contrast (a) . Bar: 100 μm. *Bereiter-Hahn J. Cell Biol. 1979*

Quantitative reflection contrast microscopy of living cells

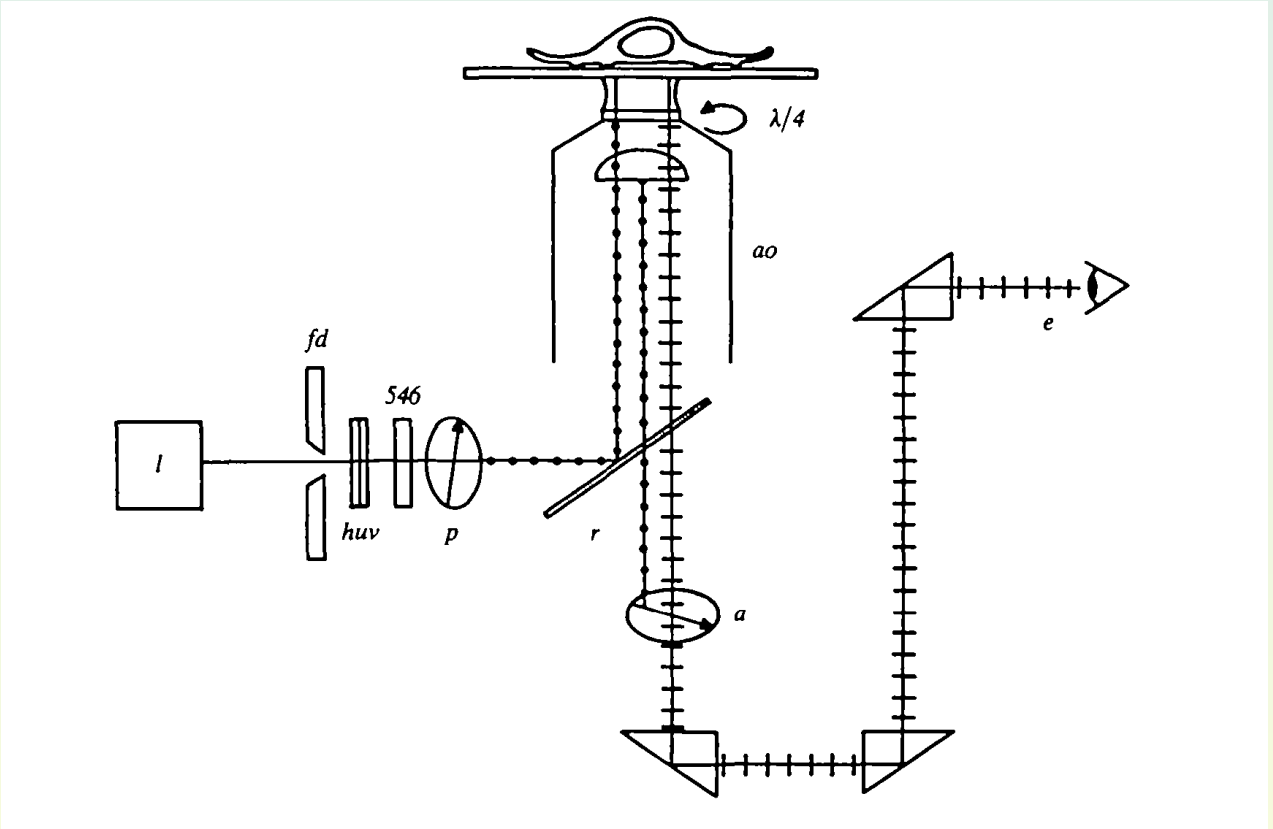

Optical setup and pathways of an interference microscope. fd:field diaphragm, huv filters, p: polarizer, r: semi-reflecting mirror, ao: antireflex objective with a rotatable $\lambda/4$ quartz plate (45^o), a: analyzer (at 90^o from p), e: camera. *Verschueren H., J.Cell Sci. 1985*

Quantitative reflection contrast microscopy of living cells

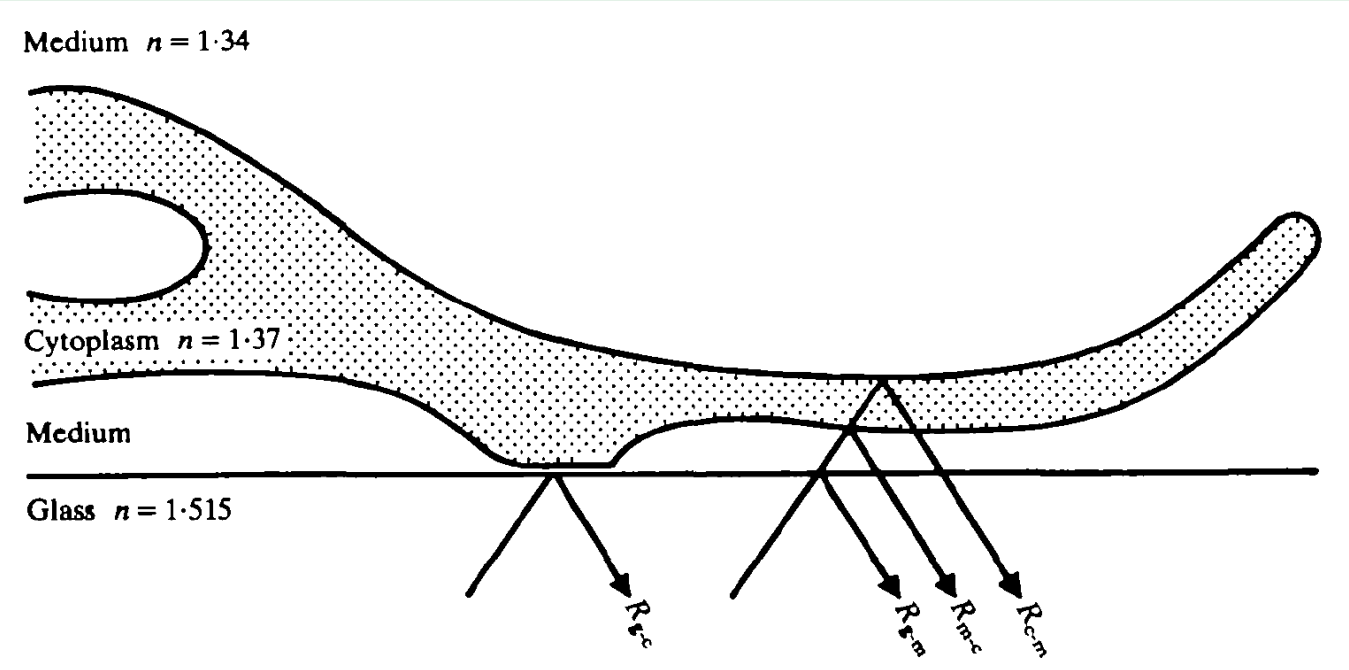

The reflected beams depend on the cell layer and can interfere with each other.
Verschueren H., J.Cell Sci. 1985

Quantitative reflection contrast microscopy of living cells

The intensity J of a composite beam resulting from interference of two beams reflected at different interfaces (glass/medium or medium/cell) can be calculated by the expression: *Bereiter-Hahn J. Cell Biol. 1979*

$$J = \left(\frac{n_g - n_m}{n_g + n_m} \pm \frac{n_c - n_m}{n_c + n_m} \times \cos \frac{4\pi n_m \cdot d \cos \beta}{\lambda} \right)^2 + \left(\frac{n_c - n_m}{n_c + n_m} \times \sin \frac{4\pi n_m \cdot d \cos \beta}{\lambda} \right)^2 \quad (3)$$

β = the angle of incidence at the reflecting surface .
$\pm$ means $(-)$ phase shift of $\lambda/2$ for the reflection from optically denser medium, i .e., at a medium/cell interface, $(+)$ interface with reflecting medium of lower refractive index, i .e ., the glass/medium interface. d = distance between glass and cell surface filled with culture medium with the refractive index n_m .

Optical methods for probing living tissues non intrusively: OCT

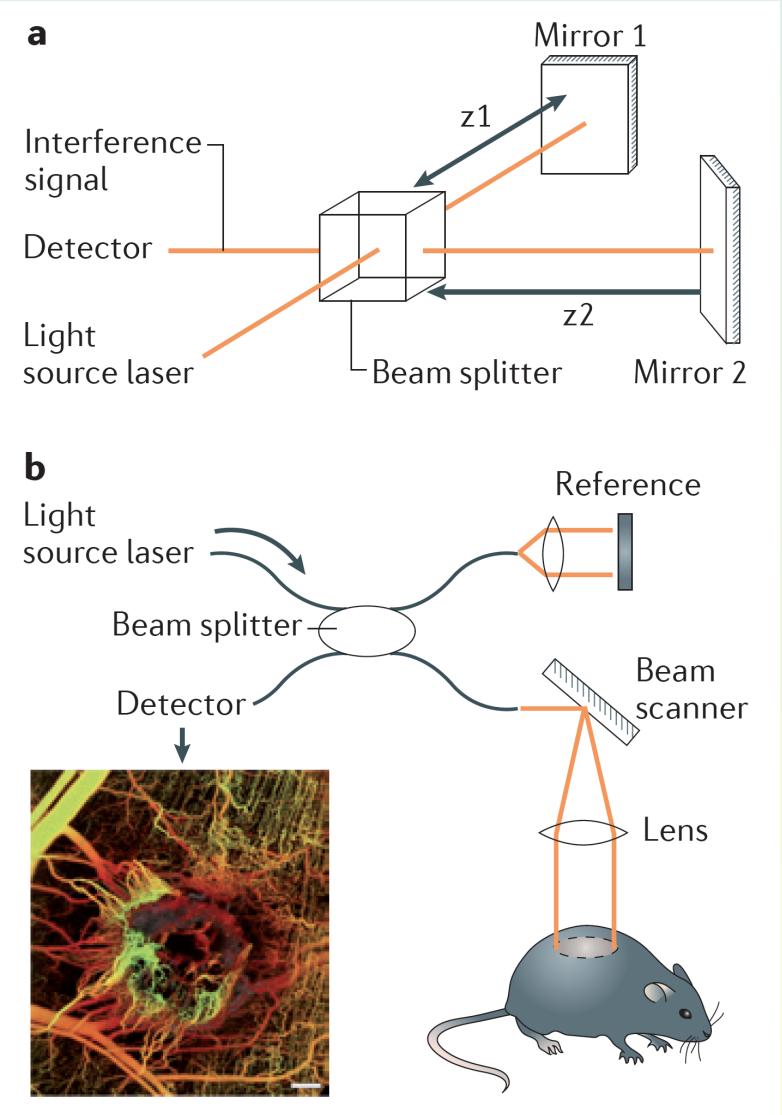

OPTICAL COHERENCE TOMOGRAPHY (OCT),
Interferometry is extended in OCT to tissues: as the beam propagates into the tissue, scattering by cells and other structures redirects some light backwards. This scattered light is collected and made to interfere with the second (mirror-reflected) beam. Using the resulting interference signal, the depth of all the tissue-scattered light can be measured to the limit of the resolution of the interferometer, which is typically $5-10\ \mu$m in OCT systems.
[Vakoc, Nat. Rev. Cancers 2012]

Imaging of tumour angiogenesis using OCT

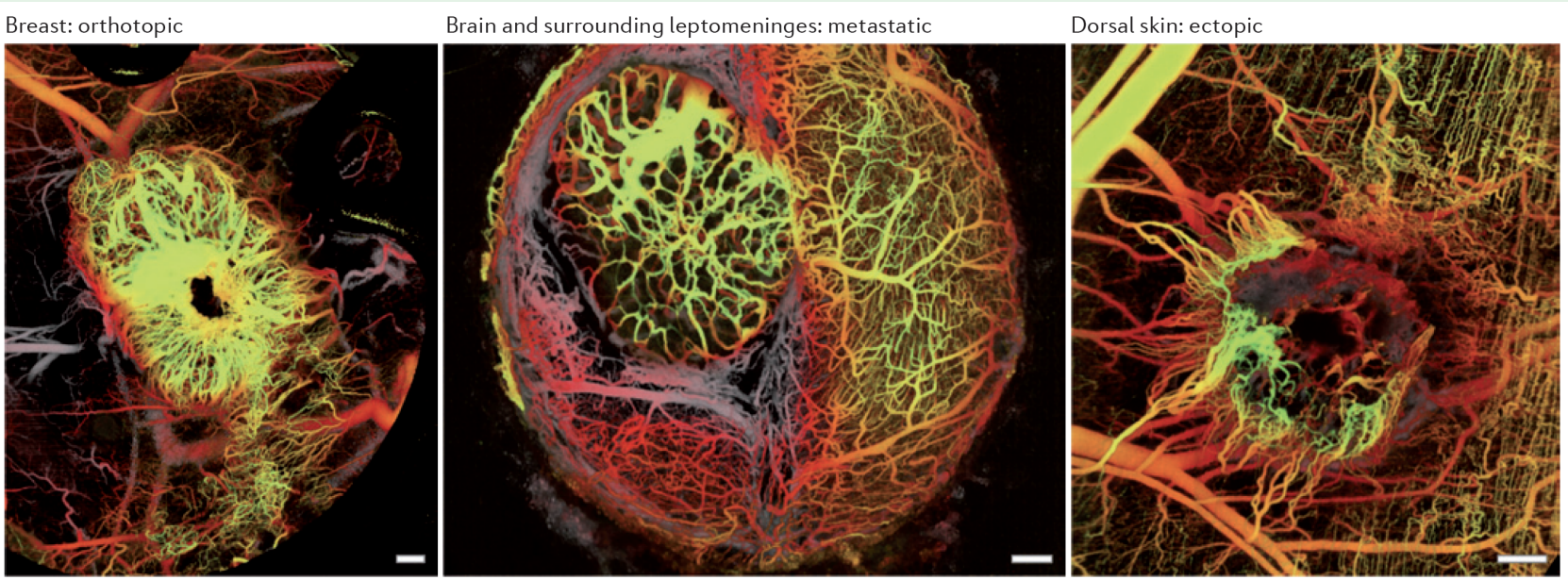

Optical coherence tomography (OCT)-based angiography reveals strikingly different vascular networks in an MCaIV murine mammary carcinoma grown in different anatomical sites. The scale bars represent 500 μm. *[Vakoc, Nat. Rev. Cancers 2012]*

Looking for subcellular structures:

Scanning Electron Microscopy SEM for imaging HSCs and MSCs

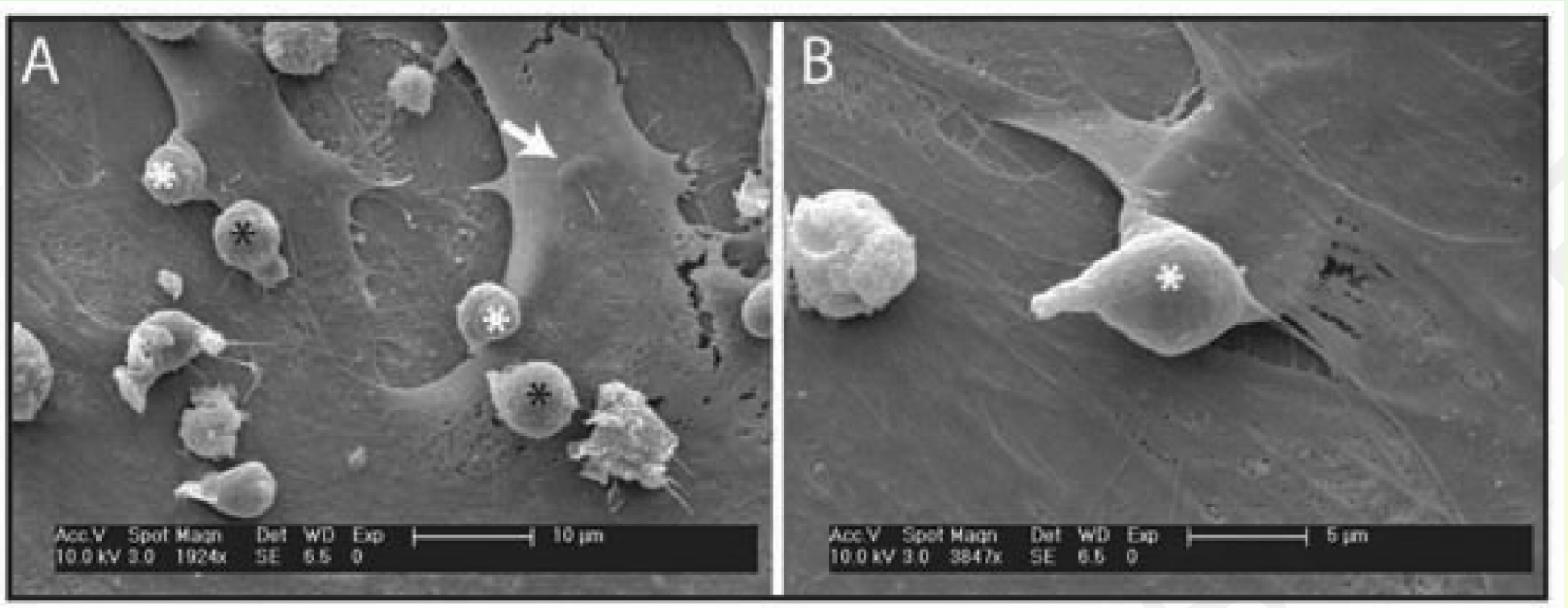

Scanning electron microscopy analysis revealed that HSC are either above the MSC layer (black asterisks) or beneath (white arrow). *[Jing et al. Haematologica 2010]*

Resolution limit: Rayleigh criteria

Definition

Rayleigh criteria gives the resolution limit of a conventional microscope:

- Lateral resolution : $d_{x,y} = \frac{0.61\lambda}{NA}$
- Axial resolution : $d_z = \frac{2\lambda}{NA^2}$
- $\lambda = 633\text{nm}$, $NA = 1.4 : d_{x,y} = 276\text{nm}$;
  $NA = 1.65 : d_{x,y} = 234\text{nm}$;
- $\lambda = 633\text{nm}$, $NA = 1.4 : d_z = 645\text{nm}$;
  $NA = 1.65 : d_z = 465\text{nm}$;

Diffraction phase microscopy of living cells

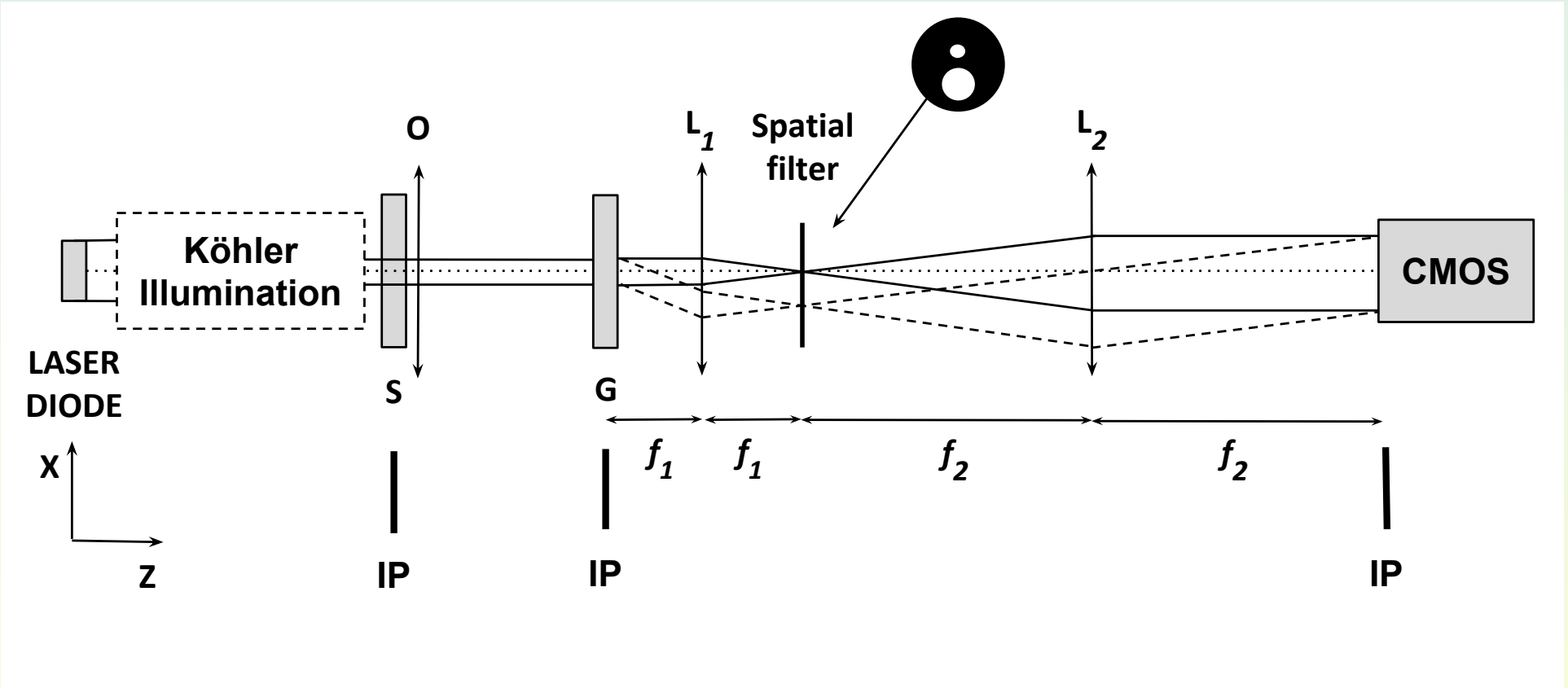

QPM set-up. A transmission grating (G), positioned at the image plane (IP) of the microscope objective lens (O), is used for beam division into a central beam (order 0) and two symmetric beams (order 1) with respect to the optical axis. A spatial filter is placed at the Fourier plane of the lens L1 to select the 1st order beam (imaging field) and to low-pass filter the 0th order beam. The two beams are recombined with the lens L2 and the interferogram is recorded on a CMOS camera. (C. Martinez-Torres, submitted to J. Biomed. Optics 2013)

Diffraction phase microscopy: Fourier spectra of interferometric images

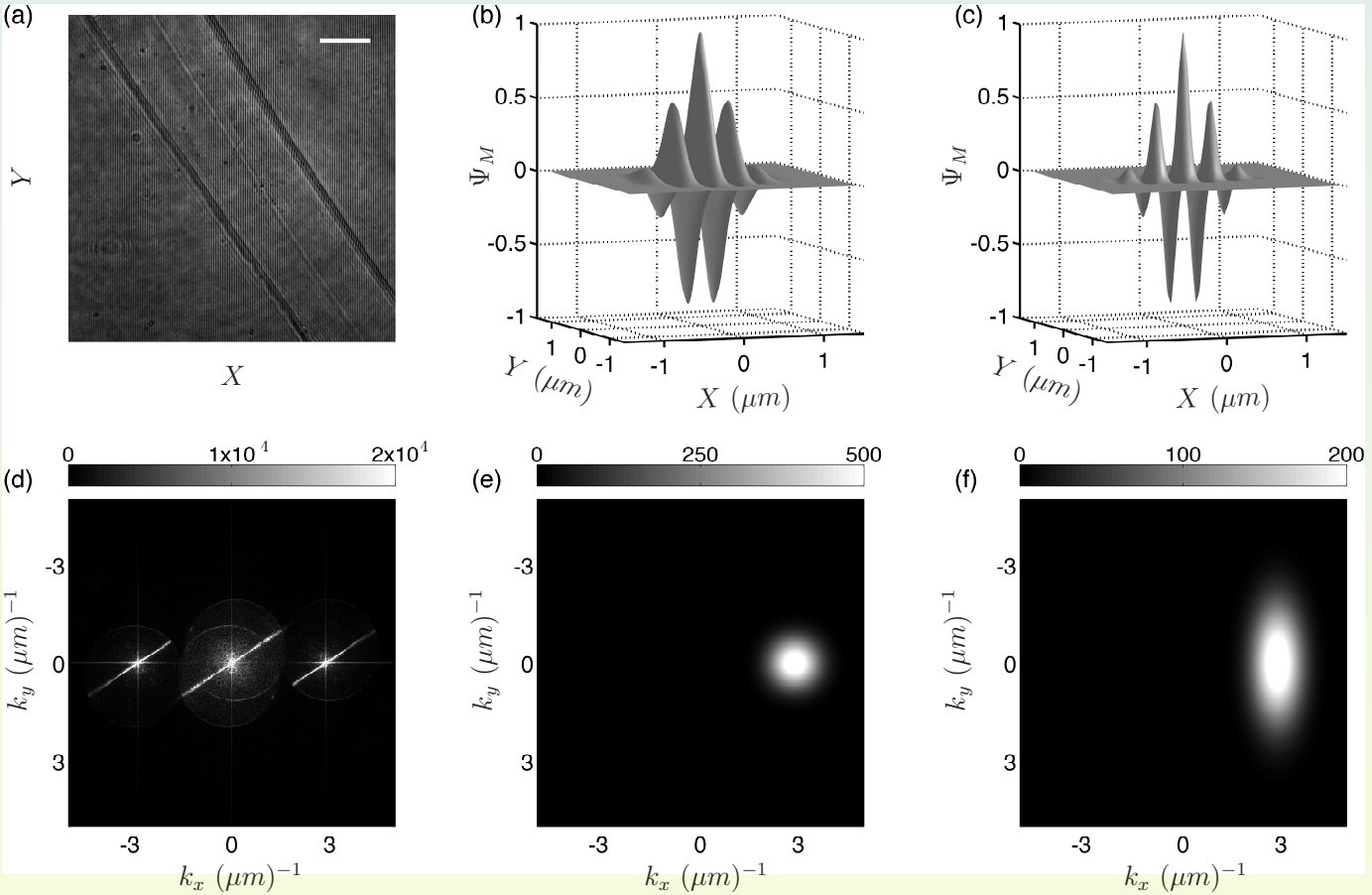

(a) Untreated QPM image of a glass coverslip coated with polymer layer including a scratch in the diagonal direction. The scale bar is 10 μm. (b) Real part of the symmetric two-dimensional Morlet wavelet Ψ_M with $\epsilon = 1$. (c) Real part of the anisotropic two-dimensional Morlet wavelet Ψ_M, with $\epsilon = 10$. (d), (e) and (f) Modulus of the 2D Fourier transforms of (a), (b), and (c) respectively, coded with a grey colormap. (C. Martinez-Torres, submitted to J. Biomed. Optics 2013)

Diffraction phase microscopy: the model for the intensity maps

The intensity map $I(x, y)$ recorded on the CMOS camera, is directly proportional to the modulus square of the electric field at this point:

$$I(\vec{x}) = |U_0 + U_1|^2(\vec{x}) = [|U_0|^2 + |U_1|^2 + U_0 U_1^* + U_0^* U_1](\vec{x}) \quad (1)$$

If f_g is the spatial frequency of the grating, the phase difference between U_1 and U_0 includes both the grating and the object phase information: $\Phi(\vec{x}) = f_g x + \phi(\vec{x})$, with $\vec{x} = (x, y)$. This gives a synthetic form of $I(\vec{x})$:

$$I(\vec{x}) = P(\vec{x}) + Q(\vec{x}) \cos(f_g x + \phi(\vec{x})) \, . \quad (2)$$

$\phi(\vec{x})$ is the phase due the object transmission at location $\vec{x}$. $P(\vec{x})$ and $Q(\vec{x})$ are real valued, they correspond respectively to the background and modulation intensities at location $\vec{x}$. One common assumption is that $P(\vec{x})$ and $Q(\vec{x})$ vary much slower than $\phi(\vec{x})$.

Diffraction phase microscopy: the model for the intensity maps

The local frequencies of the signal U can be computed in both directions x and y from the partial derivatives of the phase $\phi(\vec{x})$:

$$f_x(\vec{x}) = f_g + \partial[\phi(\vec{x})]/\partial x \ , \tag{3}$$

$$f_y(\vec{x}) = \partial[\phi(\vec{x})]/\partial y \ . \tag{4}$$

These equations can be rewritten in the vectorial form:

$$\begin{bmatrix} f_x \\ f_y \end{bmatrix} = \vec{\nabla}(f_g x + \phi(\vec{x})) \ . \tag{5}$$

Eq. (3) shows that the local frequency in x may deviate from the carrier frequency f_g depending on the strength of the phase derivative with respect to x, the steeper $\phi(\vec{x})$, the larger this deviation.

Diffraction phase microscopy: wavelet analysis for retrieving phase contours

The two-dimensional continuous wavelet transform (CWT) of $I(\vec{x})$ with $\vec{x} = (x, y)$ is defined as [J.P. Antoine et al. 2004]:

$$W_\Psi(\vec{b}, a, \theta) = a^{-\eta} \int_{\Re^2} I(\vec{x})\, \Psi^* \left(a^{-1} r_\theta(\vec{x} - \vec{b}) \right) \mathrm{d}^2\vec{x}\,. \qquad (6)$$

$W_\Psi(\vec{b}, a, \theta)$ is the wavelet transform coefficient,

$\vec{b} = (b_x, b_y)$ is a 2D translation parameter describing the position of the wavelet,

$a > 0$ is the scale dilation parameter (non dimensioned),

θ is a rotation parameter, $\mathbf{r}_\theta$ is the 2×2 rotation operator matrix,

Ψ is the mother wavelet, Ψ^* the complex conjugate of Ψ, η is a normalization exponent.

In Fourier space:

$$W_\Psi(\vec{b}, a, \theta) = a^{\eta} \int_{\Re^2} \widehat{I}(\vec{k})\, e^{i\vec{b}\cdot\vec{k}}\, \widehat{\Psi}^* \left(a\, r_{-\theta}(\vec{k}) \right) \mathrm{d}^2\vec{k}\,. \qquad (7)$$

Diffraction phase microscopy: wavelet analysis for retrieving phase contours

We use the 2D Morlet wavelet to detect localized and oriented features in the interferometric images:

$$\Psi_M(\vec{x}) = e^{i\vec{k_0}\cdot\vec{x}} e^{-\frac{1}{2}|A\vec{x}|^2} - e^{-\frac{1}{2}|A^{-1}\vec{k_0}|^2 - \frac{1}{2}|A\vec{x}|^2}, \quad (8)$$

$$\widehat{\Psi}_M(\vec{k}) = \sqrt{\varepsilon}[e^{-\frac{1}{2}|A^{-1}(\vec{k}-\vec{k_0})|^2} - e^{-\frac{1}{2}|A^{-1}\vec{k_0}|^2 - \frac{1}{2}|A^{-1}\vec{k}|^2}]. \quad (9)$$

k_0 is the wave vector,
$A = diag[1, \varepsilon^{1/2}]$ is a 2×2 anisotropic matrix ($\varepsilon \geq 1$).
In simpler form:

$$\Psi_M(\vec{x}) = \exp[-\frac{1}{2}(x^2 + \varepsilon y^2)](\exp(ik_0 x) - \exp(-k_0^2/2)) . \quad (10)$$

Diffraction phase microscopy: 2D Morlet wavelets

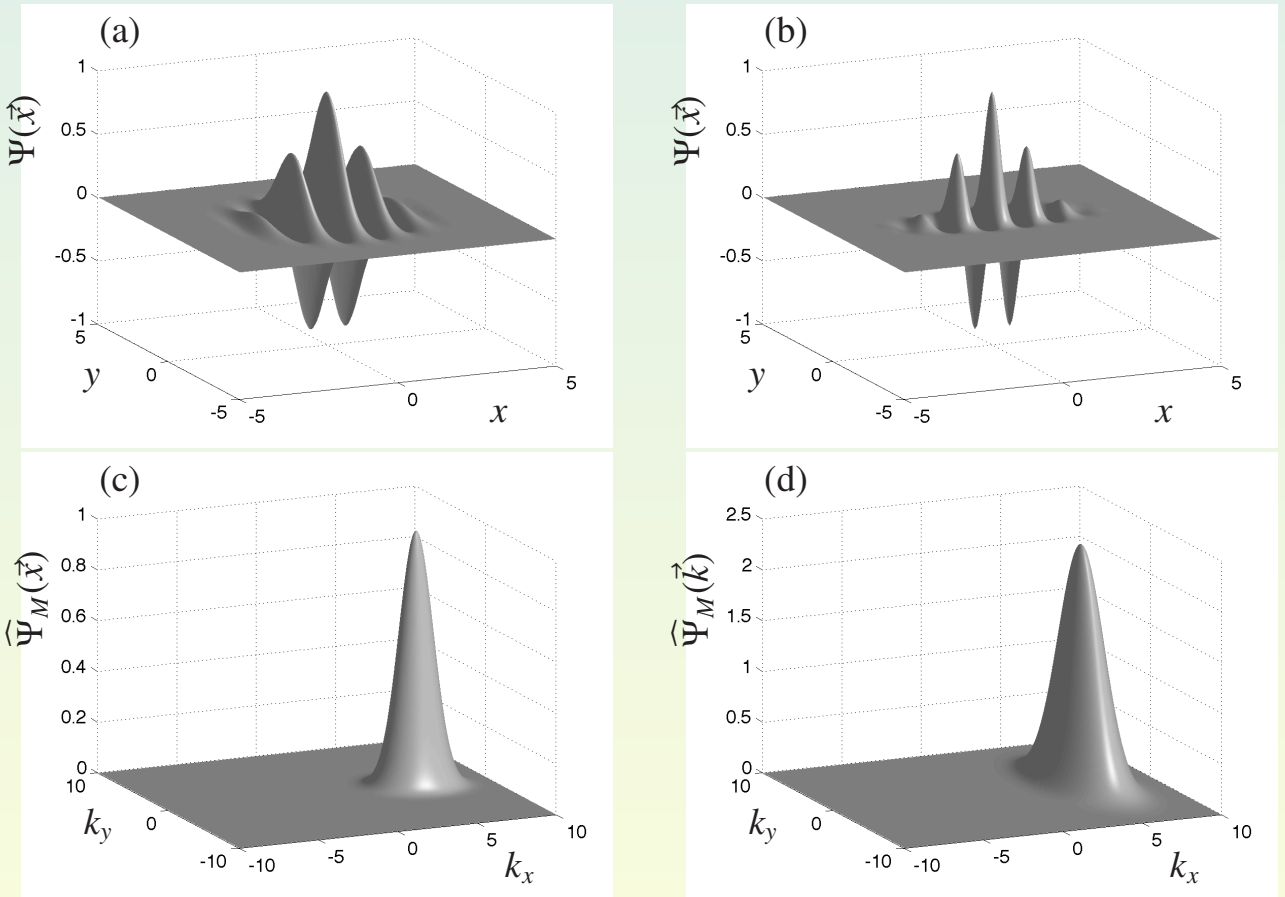

2D anisotropic Morlet wavelet have been tested to uncover the periodic modulations of the fringe patterns captured on the QPI system. With this method, we have also been able to retrieve the phase, with the WT modulus maxima method.

Diffraction phase microscopy: anisotropy of the wavelets

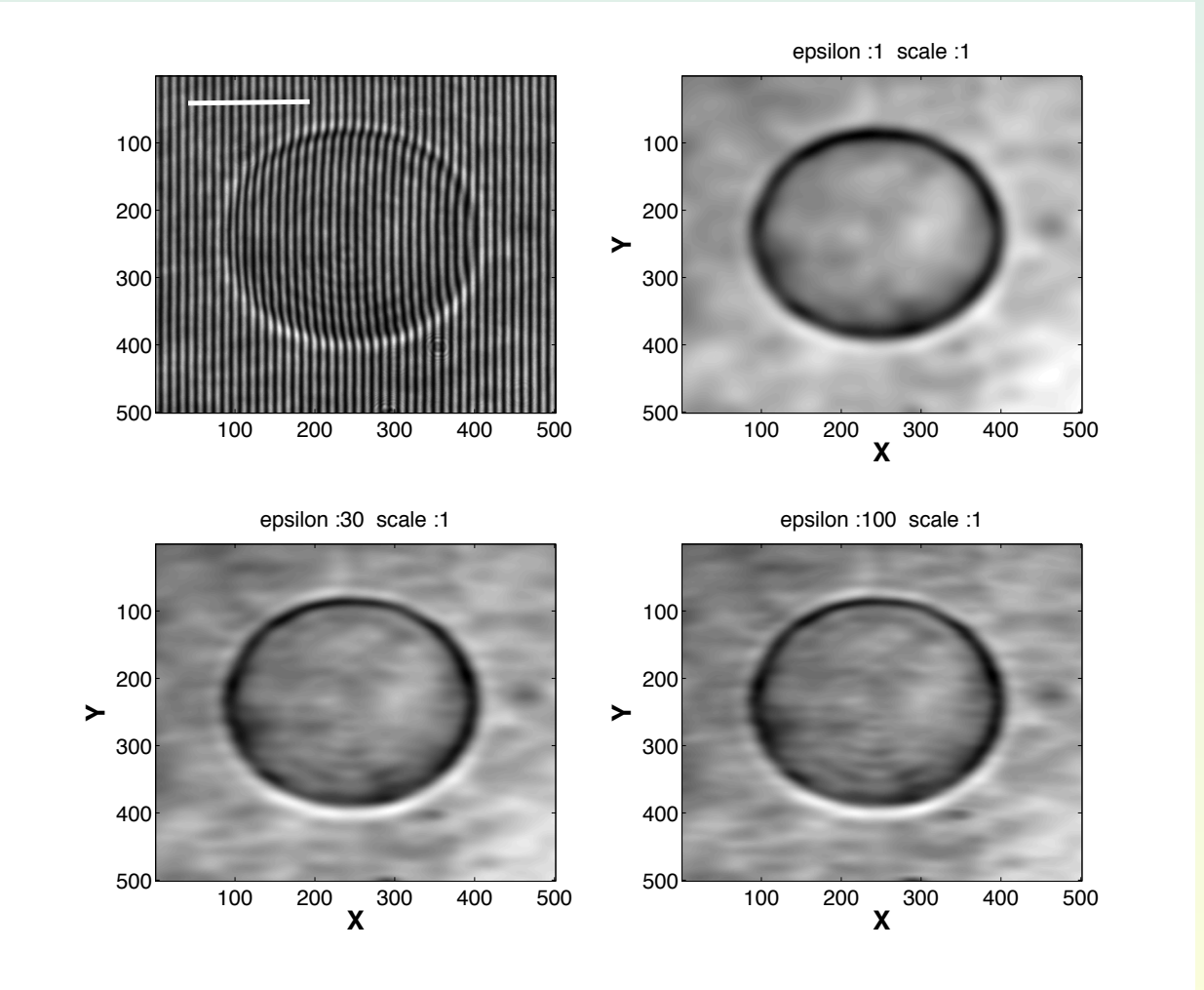

The anisotropic 2D Morlet wavelet with $\varepsilon = 30$ is more efficient to capture the contours of this latex bead than the isotropic one.

Diffraction phase microscopy: the wavelet ridge

The ridge of the wavelet transform corresponds to the scales $a_r(\vec{b})$ where the local derivative of the wavelet phase ϕ_Ψ compensates the local derivative of the object phase ϕ:

$$[f_g + \vec{\nabla}\phi(\vec{x})] - \vec{\nabla}\phi_\Psi(a_r^{-1}(\vec{b})\, r_\theta(\vec{x} - \vec{b})) = 0\ . \tag{11}$$

If $I(\vec{x}) = Q(\vec{x})\exp(i\phi(\vec{x}))$, with $Q(\vec{b}) \simeq Cst$, we get the form of the wavelet coefficients:

$$W_\Psi(\vec{b}, a) = \frac{\widehat{\Psi_M}[a(f_g(1,0) + \vec{\nabla}\phi(\vec{b}))]}{C(\vec{b}, a)} Q(\vec{b}) e^{i\phi(\vec{b})}\ , \tag{12}$$

up to a correction term $C(\vec{b}, a)$ that depends on the local variations of the phase $\phi(\vec{x})$ and the modulation amplitude $Q(\vec{x})$ of the optical signal on the ridge skeleton.

Diffraction phase microscopy: the wavelet ridge

Hence from Eq. (9) the maxima of the modulus of the CWT correspond to the wavelet ridge skeleton, where the optical phase ϕ produced by the object fulfills the equation:

$$\vec{k_0}/a_r(\vec{b}) = f_g(1,0) + \vec{\nabla}\phi(\vec{b}) \ . \tag{13}$$

The modulus of the wavelet transform on the ridge skeleton reads:

$$W_\Psi(\vec{b}, a_r(\vec{b})) = \frac{\widehat{\Psi_M}(\vec{k_0})}{C(\vec{b}, a_r(\vec{b}))} Q(\vec{b}) \ e^{i\phi(\vec{b})} \ . \tag{14}$$

Diffraction phase microscopy: looking for the modulus maxima of the wavelet transform

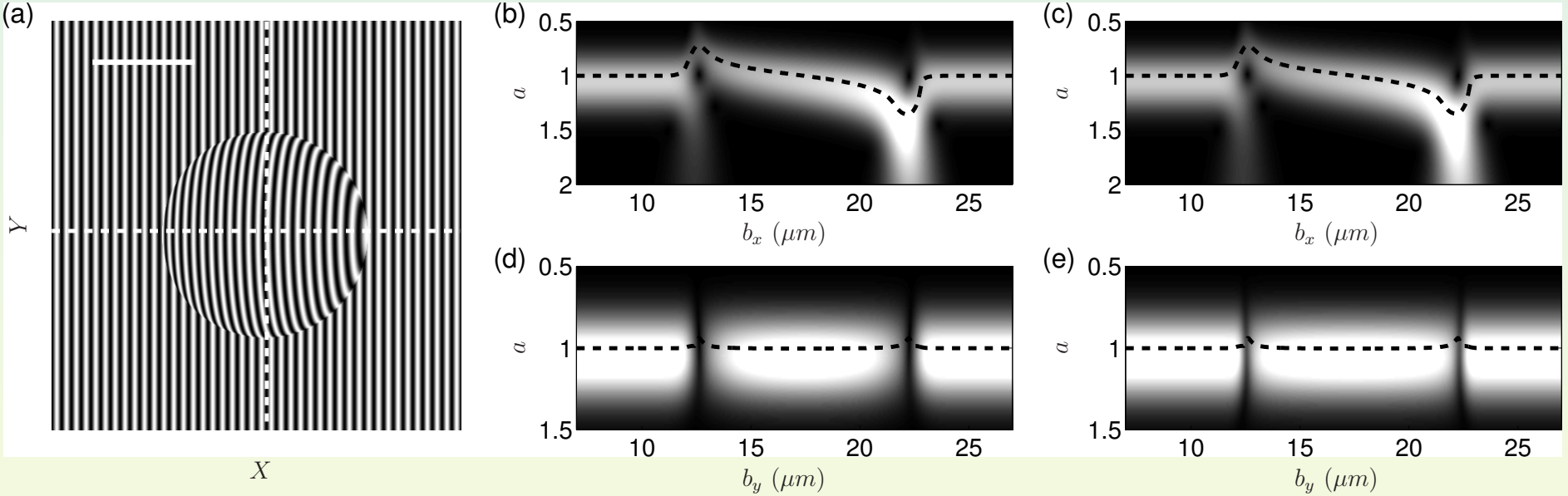

((a) Theoretical interferometric image of a transparent micro-bead. The scale bar is 5 μm. (b) and (d): Modulus of the 2D CWT on the horizontal (fixed Y) section shown in (a) by a white dashed line. (c) and (e): Modulus of the 2D CWT on the vertical (fixed X) section shown in (a) by a white dashed line. (b) and (d) $\varepsilon = 1$, (e) and (e) $\varepsilon = 10$.

Diffraction phase microscopy: the wavelet ridge

We compare three methods for computing the phase:

- (I) FOURIER FILTERING METHOD I: We use the 2D Morlet wavelet as a Fourier filter, with a fixed scale $a = 1$ corresponding to the grating fringe modulation f_g, it does not use the ridge detection.
- (II) RIDGE INTEGRAL METHOD II: We the 2D CWT ridge detection method to compute the phase derivative of the fringe pattern and make an integration of this derivative along X.
- (III) RIDGE ARGUMENT METHOD III: We use the 2D CWT ridge detection method to compute the new complex quantity $W_\Psi(b, a_r(\vec{b}))$ on the ridge and take its argument to compute the phase (Eq. (14)).

Diffraction phase microscopy: the ridge method optimized for the interferometric images

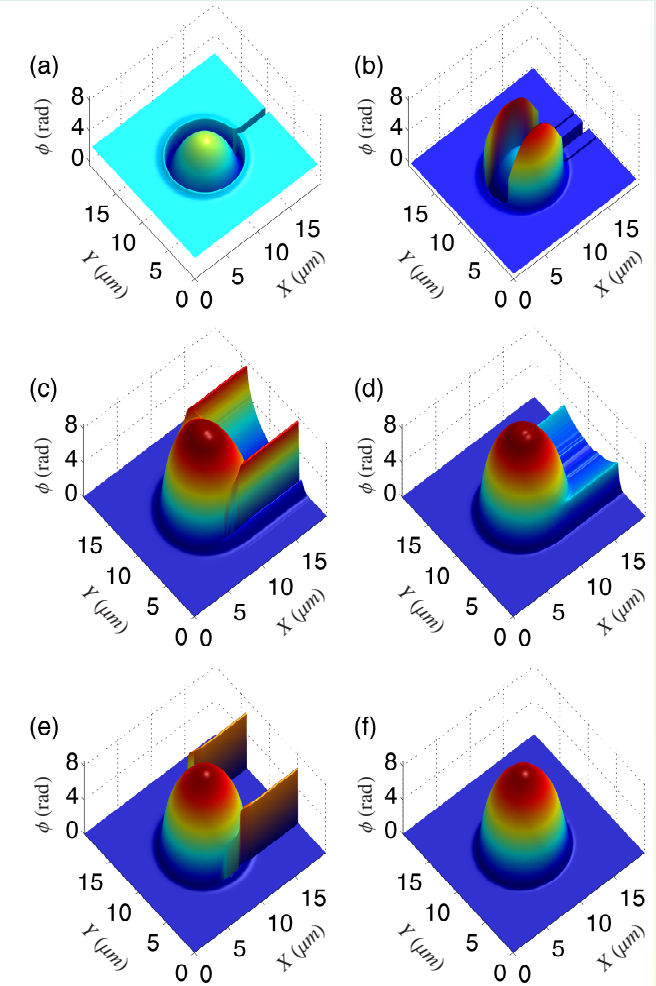

3D representation of the reconstructed phases from the fringe pattern of the theoretical bead model with methods I (a) and (b), II (c) and (d) and III (e) and (f). (a), (c), and (e) are computed with the isotropic Morlet wavelet ($\epsilon = 1$). (b), (d) and (f) are computed with the anisotropic Morlet wavelet ($\epsilon = 10$). The phase ϕ is given in radians.

Diffraction phase microscopy of a polystyrene bead

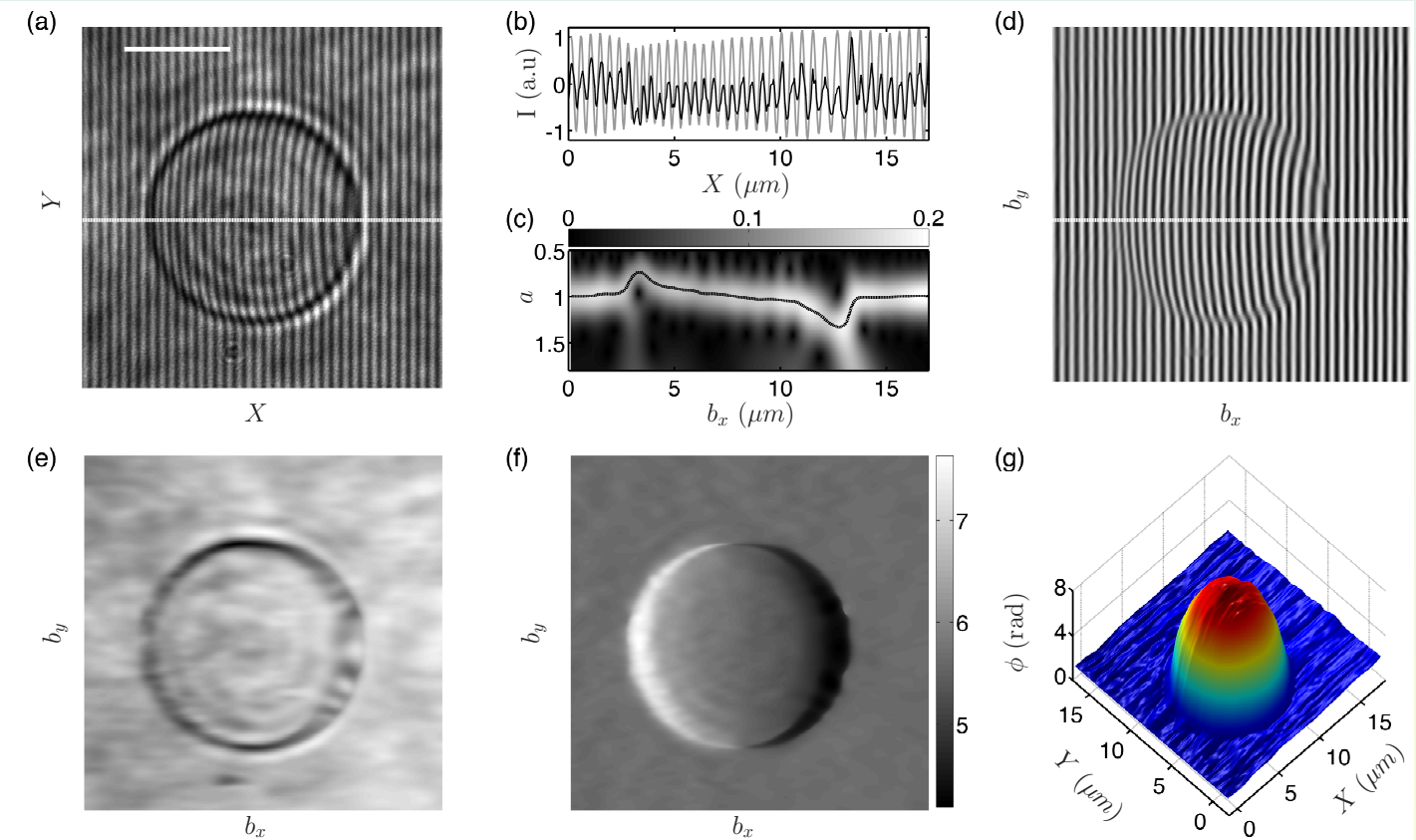

2D CWT analysis of a experimental QPM fringe pattern captured from a 5 μm radius latex micro-bead embedded in glass index matching oil. The anisotropic Morlet wavelet ($\epsilon = 10$) is used for this analysis. The grey coding is done from black (minimum) to white (maximum) (C. Martinez-Torres, J. Biomed. Optics 2014)

Diffraction phase microscopy of a spherical living myoblast

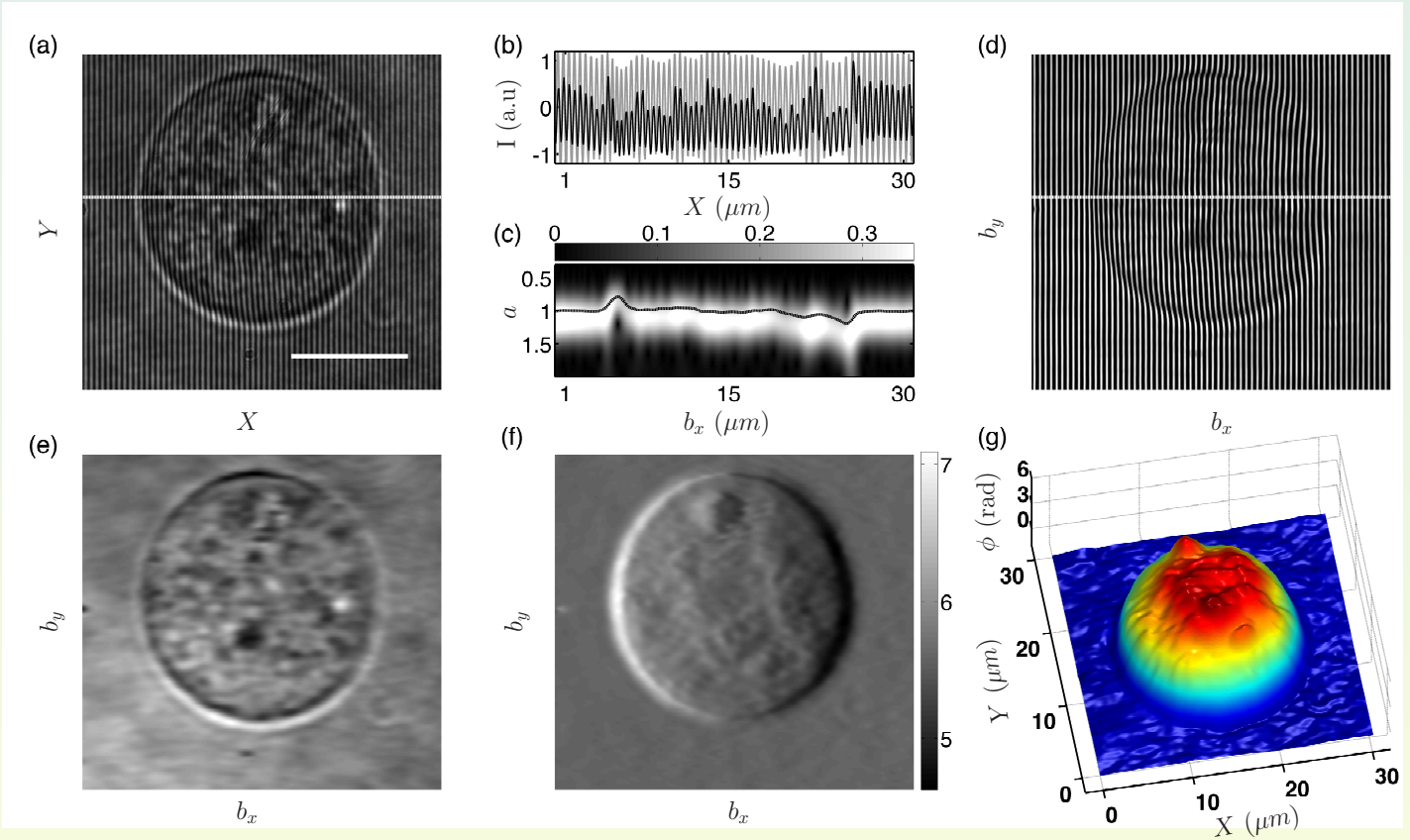

2D CWT analysis of a QPM fringe pattern collected from a round myoblast. (a) The untreated QPM image. The scale bar is 10 μm. The anisotropic Morlet wavelet ($\epsilon = 10$) is used for this analysis. The grey coding is done from black (minimum) to white (maximum) (C. Martinez-Torres, J. Biomed. Optics 2014)

Diffraction phase microscopy of a spherical living myoblast: computing the phase contours

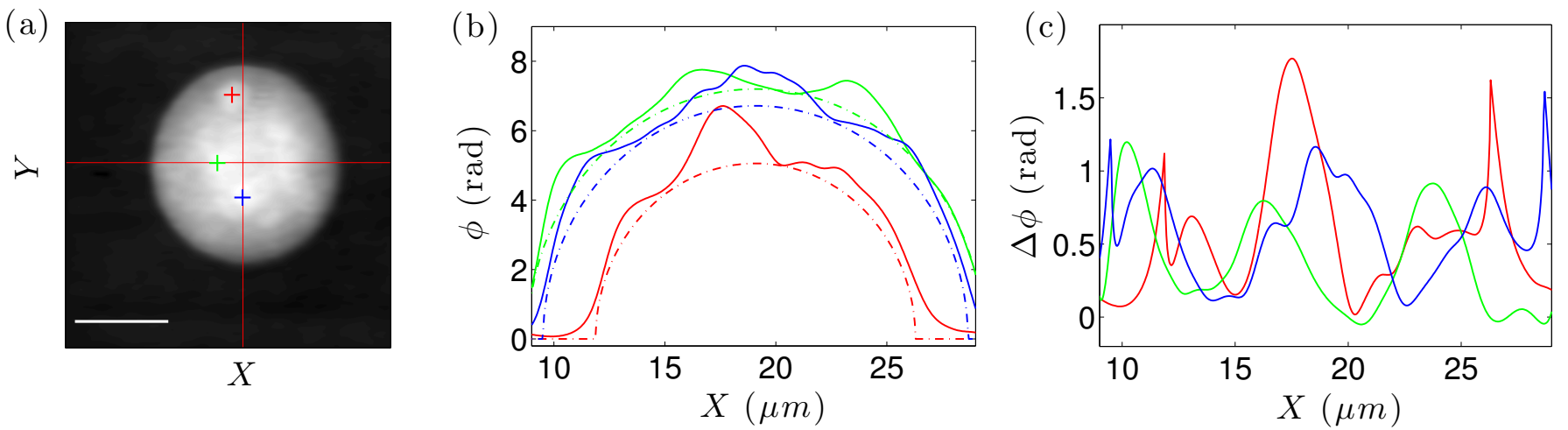

Decomposition into spherical phase shapes of the myoblast phase map (previous figure) (C. Martinez-Torres, submitted to J. Biomed. Optics 2013)

Diffraction phase microscopy of an adherent myoblast

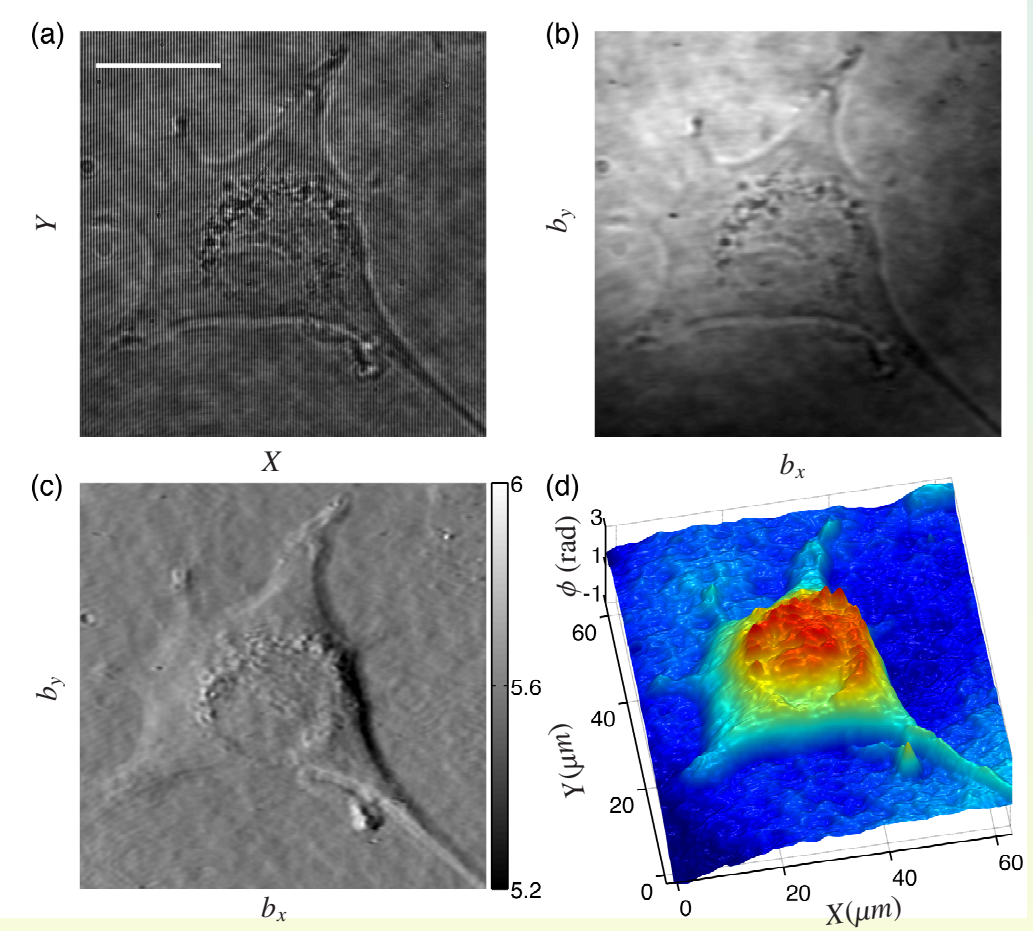

2D CWT analysis of a QPM fringe pattern collected from an adherent myoblast. (a) The untreated QPM image. The scale bar is 20 μm. The anisotropic Morlet wavelet ($\epsilon = 10$) is used for this analysis. The grey coding is done from black (minimum) to white (maximum) (C. Martinez-Torres, submitted to J. Biomed. Optics 2013)

The Chronic Myelogenous Leukemia - a disease of hematopoietic cells

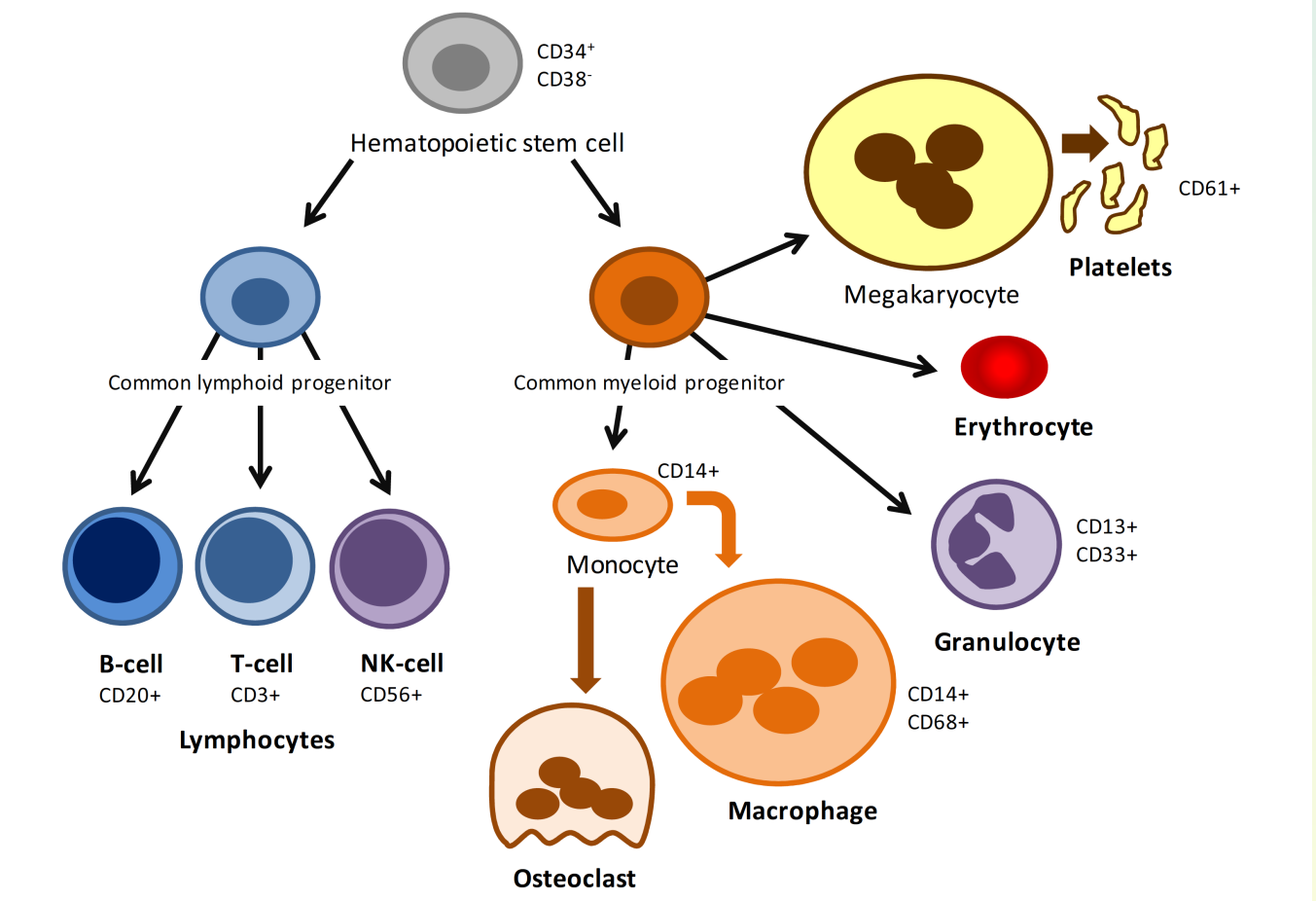

All blood cells originate from multipotent hematopoietic stem cells residing in the bone marrow. These stem cells can renew themselves and also differentiate to all cells seen in the peripheral blood. The different blood and bone marrow cells can be identified by morphology and cell surface antigens with a given cluster of designation (CD) number.

The Chronic Myelogenous Leukemia - a disease of hematopoietic cells

Chronic Myeloid Leukemia (CML) : targeted therapy model

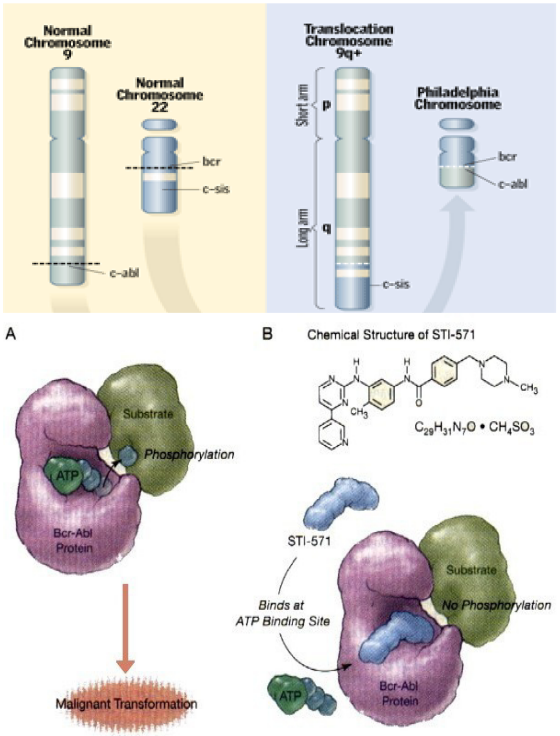

Resistance mechanisms in Chronic Myeloid Leukemia

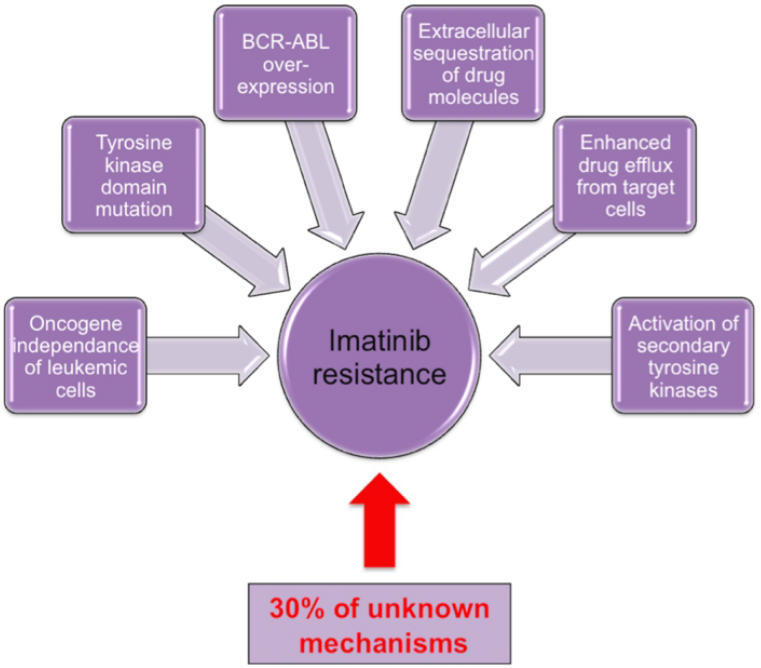

The genetic origin of CML.

The Chronic Myelogenous Leukemia - a disease of hematopoietic cells

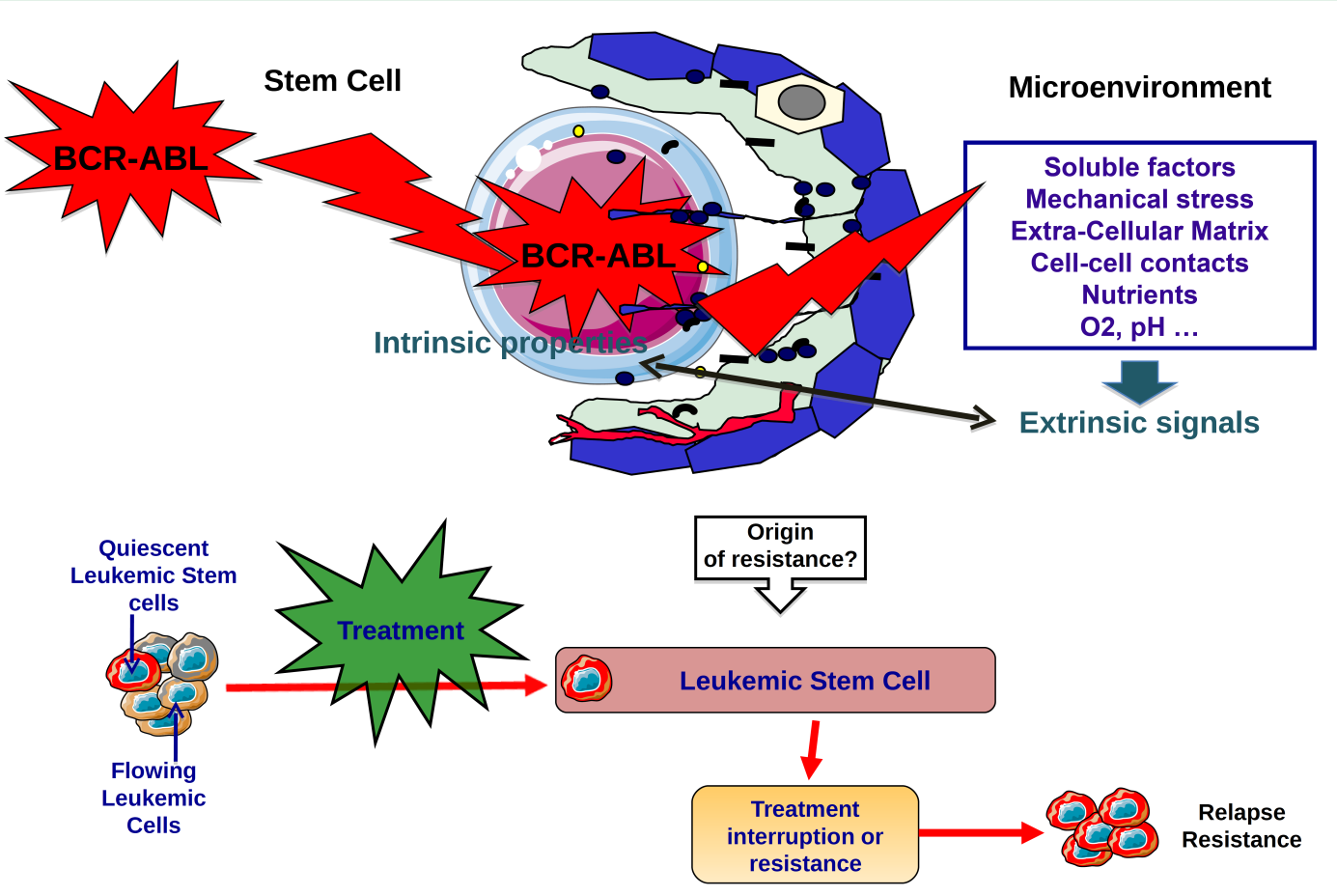

Deregulation of the niche of hematopoietic stem cells in chronic myelogenous leukemia.

Fluorescence microscopy of non adherent HSCs (heathy and cancer models)

CHRONIC MYELOGENOUS LEUKEMIA

Normal HSC

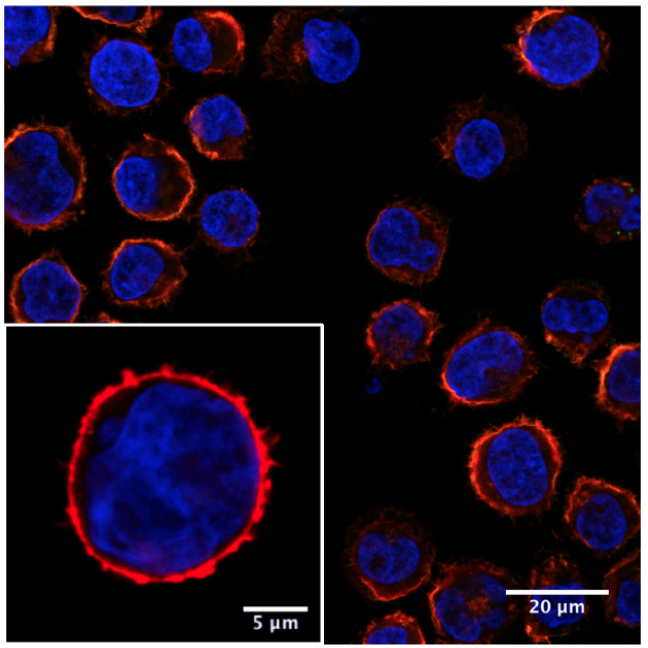

'cancer' HSC

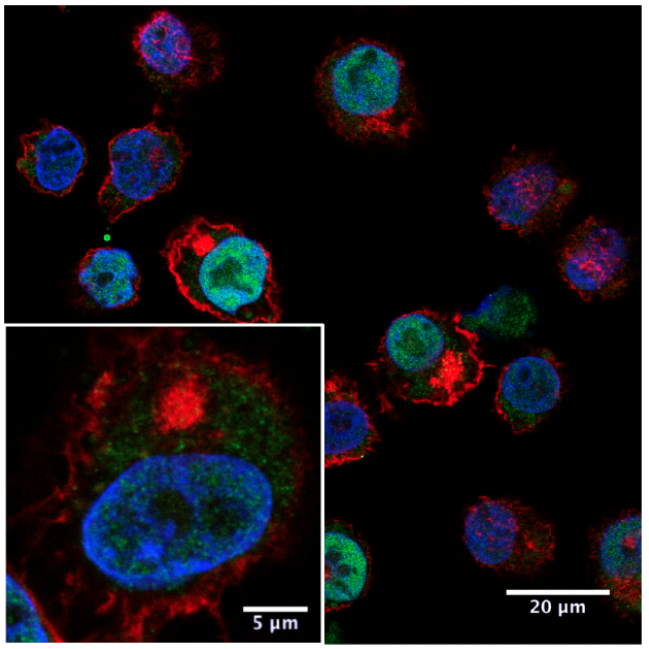

NON ADHERENT CELLS

Imaging the internal structure of non adherent hematopoietic stem cells (HSC) with fluorescence. In blue the nucleus is stained by DAPI, the actin is stained in red by phalloidin-rhodamin and GFP is stained in green (it was amplified using a rabbit polyclonal anti-GFP antibody-Alexa Fluor 488 conjugate). (B. Laperrousaz, 2013)

Fluorescence microscopy of adherent HSCs (heathy and cancer models)

CHRONIC MYELOGENOUS LEUKEMIA

Normal HSC

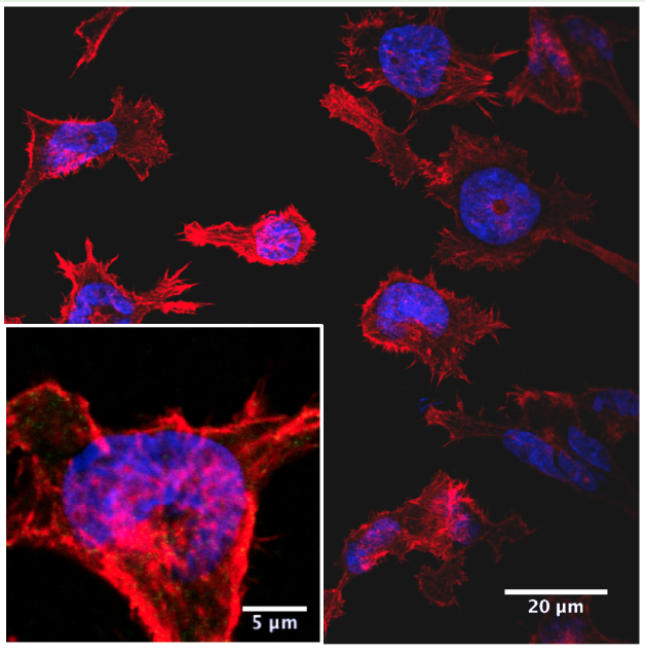

'cancer' HSC

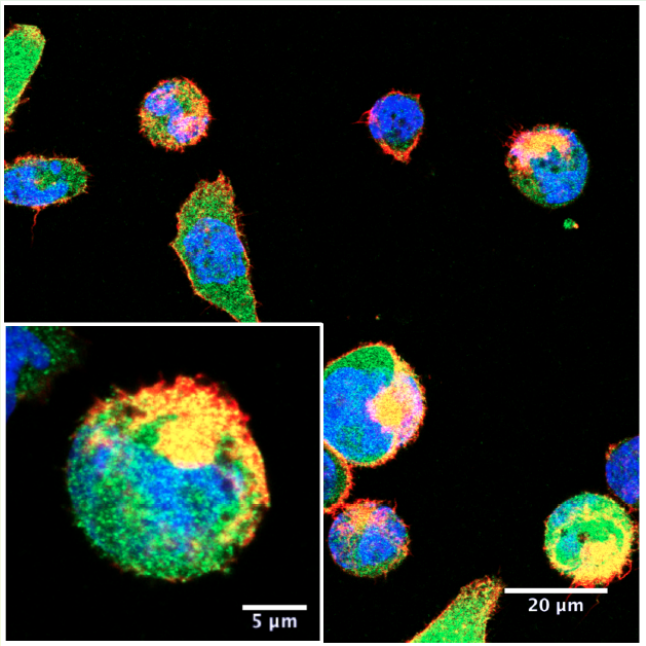

ADHERENT CELLS on FIBRONECTIN

Imaging the internal structure of hematopoietic stem cells adherent on fibronectin (HSC) with fluorescence. In blue the nucleus is stained by DAPI, the actin is stained in red by phalloidin-rhodamin and GFP is stained in green (it was amplified using a rabbit polyclonal anti-GFP antibody-Alexa Fluor 488 conjugate). (B. Laperrousaz, 2013)

QPI imaging of healthy HSCs (adherent and non adherent)

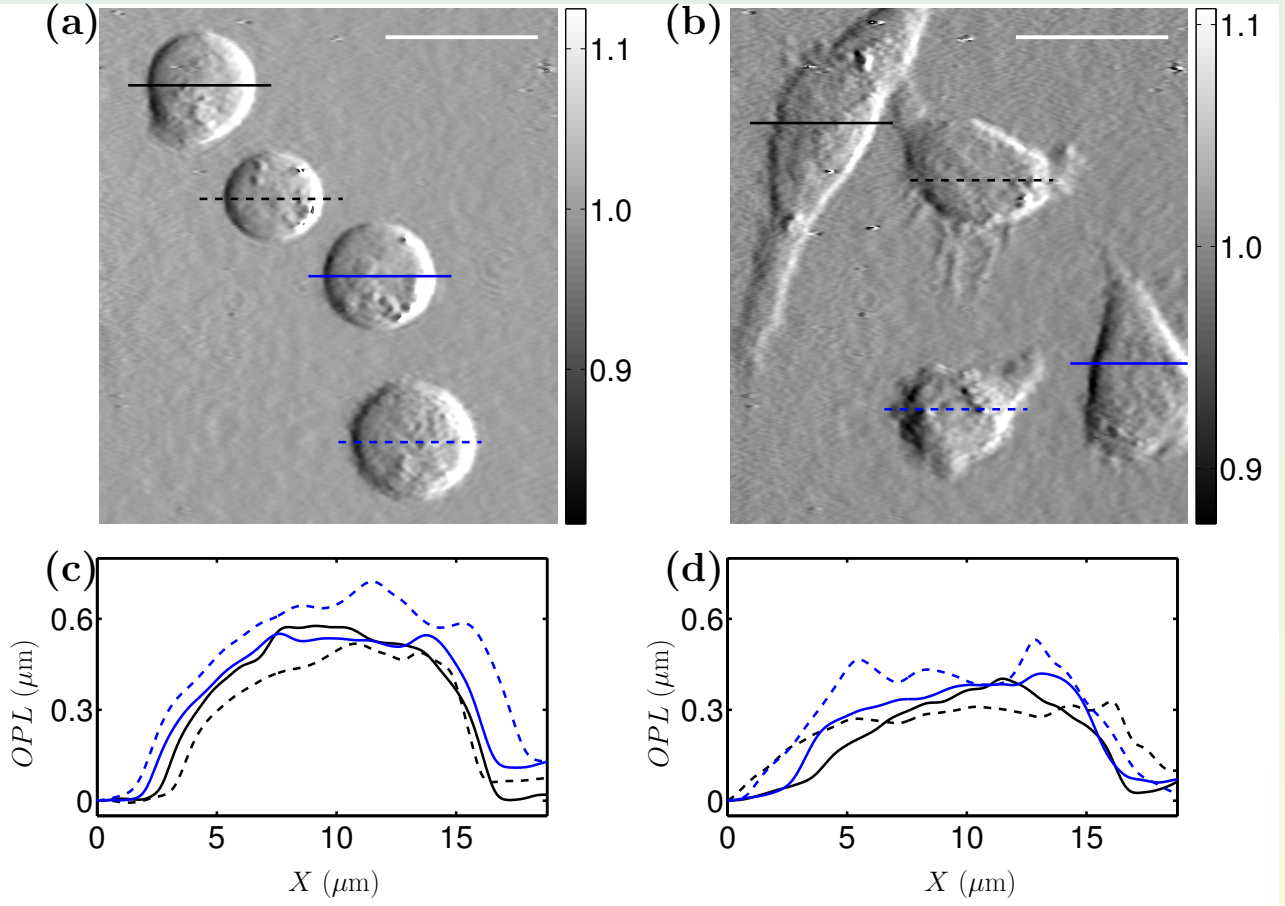

Quantitative phase images of hematopoietic stem cells (healthy). The scale bar is 20 μm. (B. Laperrousaz, 2013)

QPI imaging of cancer HSCs (adherent and non adherent)

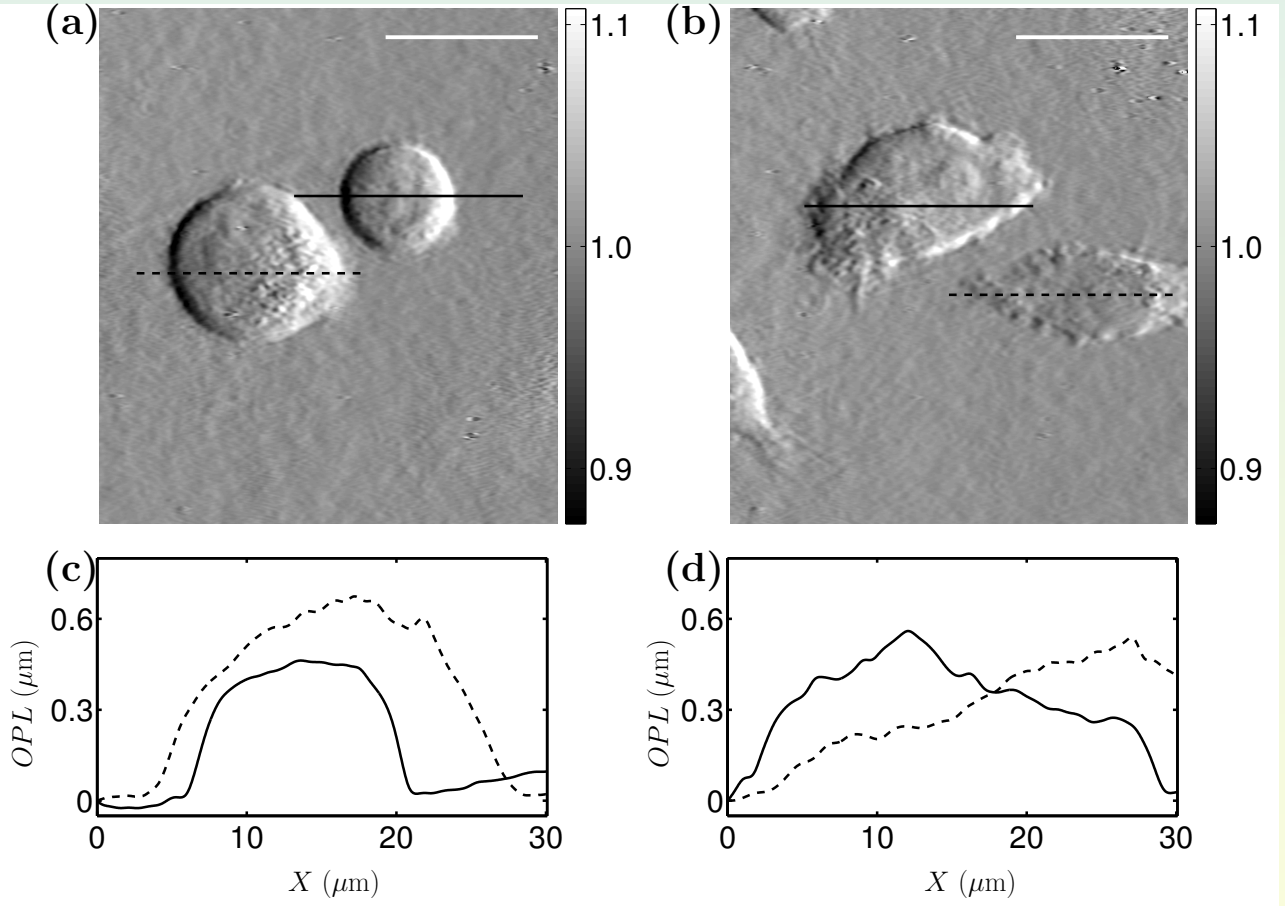

Quantitative phase images of hematopoietic stem cells (cancer). The scale bar is 20 μm. (B. Laperrousaz, 2013)

QPI imaging of cancer HSCs : looking for the dynamics of HSCs

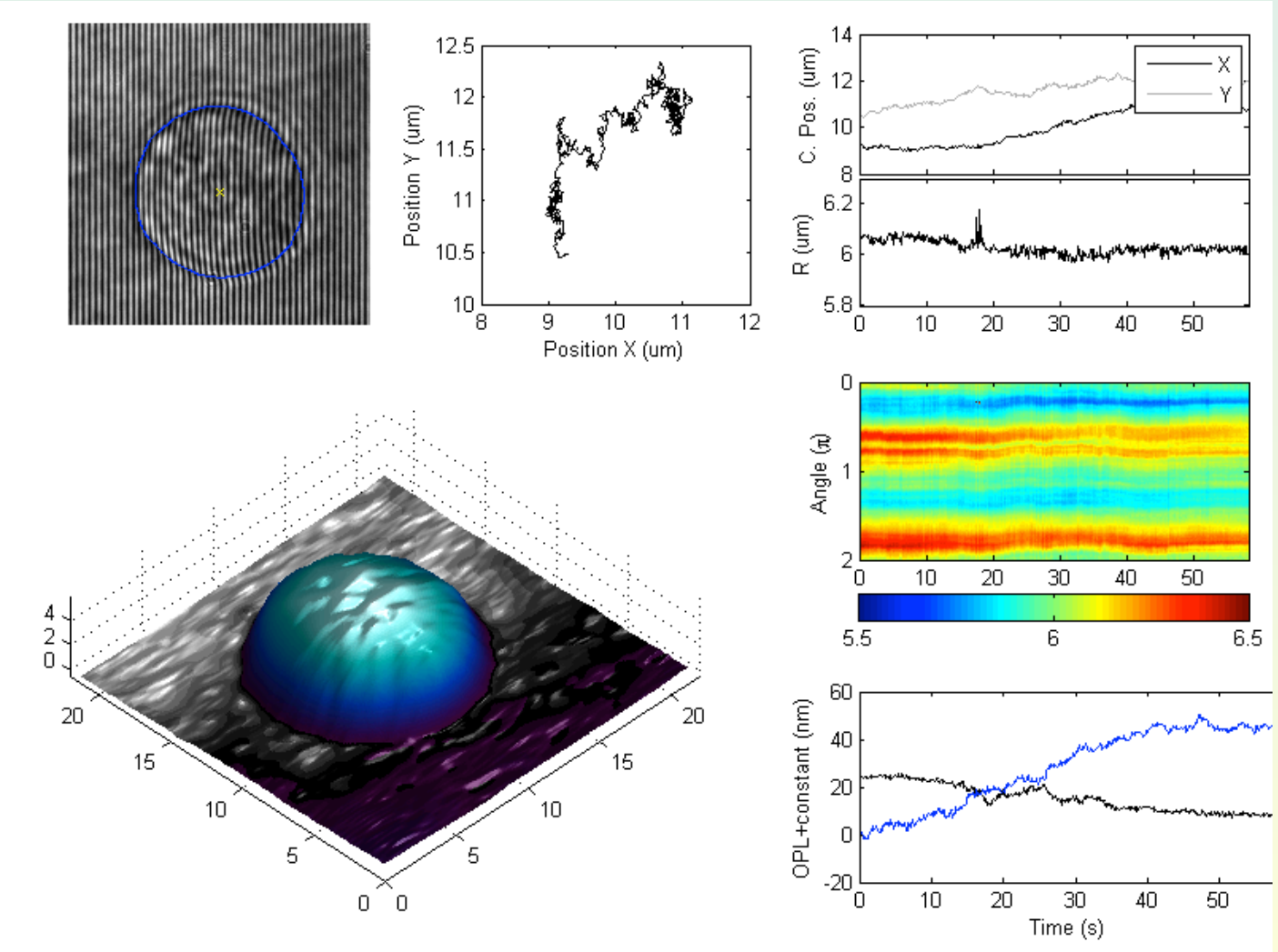

The fluctuations of position and phase are reconstructed from interferometric video films (see the video film)

QPI imaging of cancer HSCs : looking for the dynamics of HSCs

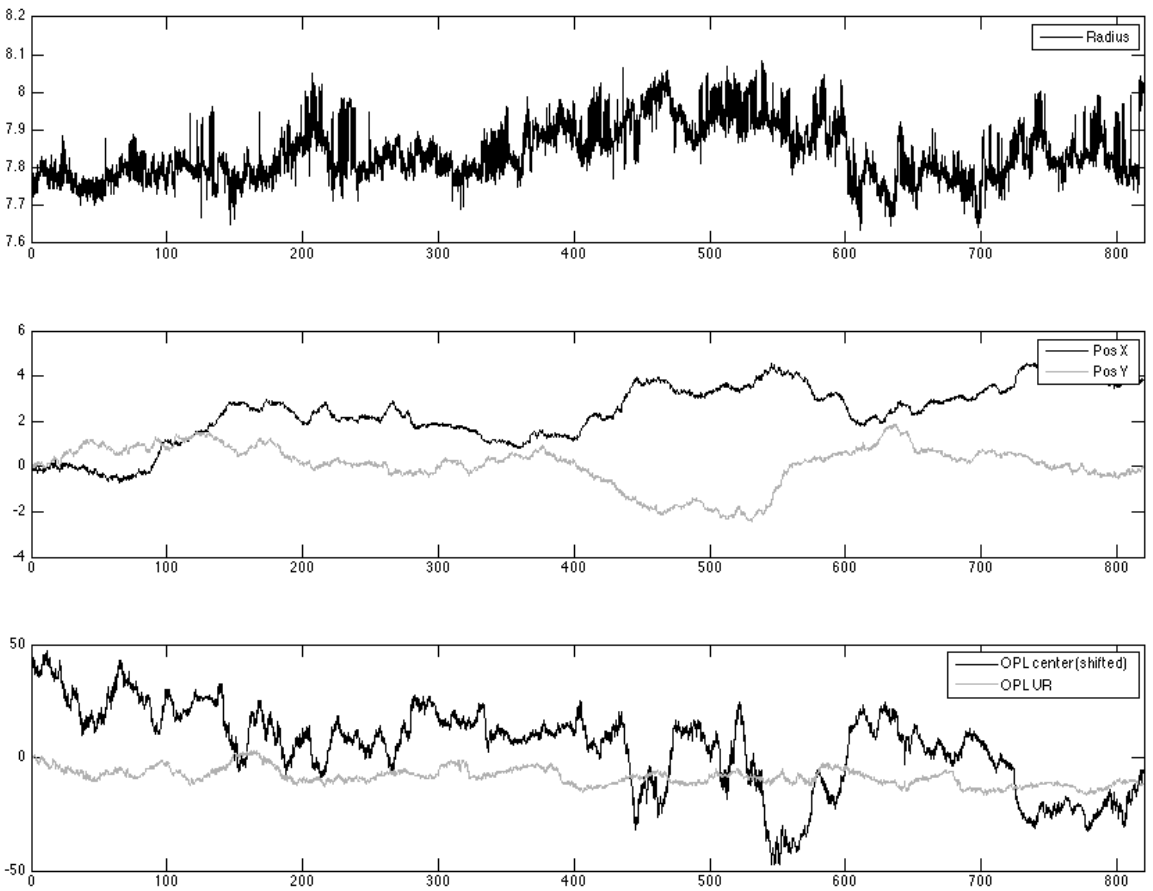

The fluctuations of position and phase are reconstructed from interferometric video films

QPI imaging of cancer HSCs : spectral analysis of the phase signals

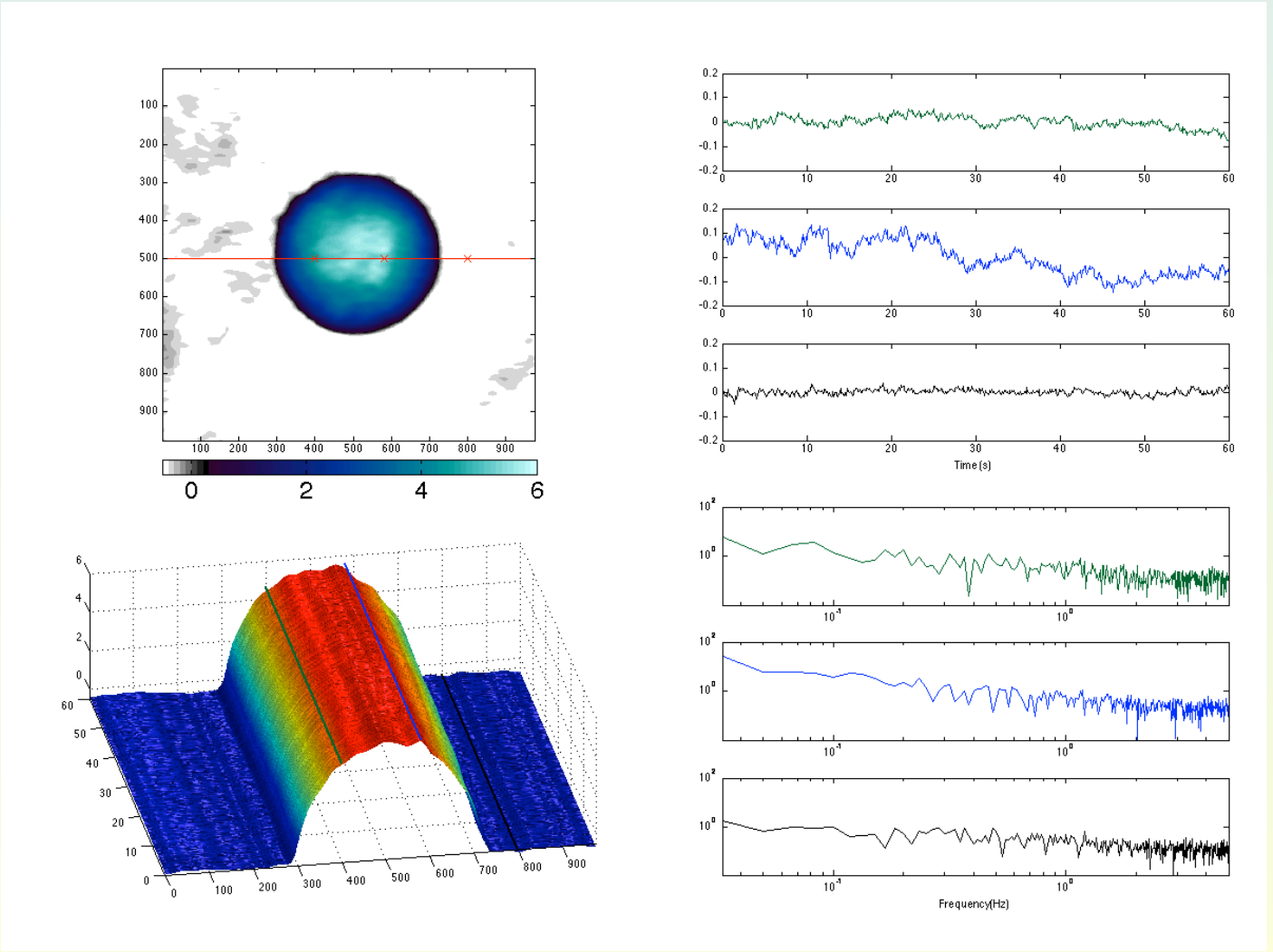

The fluctuations of the phase are analyzed in Fourier to compare with the surrounding buffer.